UNIVERSITÄT HAMBURG

Electro-optic sampling of THz pulses at the CTR source at FLASH

Diplomarbeit
von
Steffen Wunderlich
aus Siegen

vorgelegt dem
Fachbereich Physik der Universität Hamburg

angefertigt am
Deutschen Elektronen-Synchrotron DESY, Hamburg

Hamburg, März 2012

Gutachter: Dr. Jens Osterhoff (Universität Hamburg)
PD Dr. Bernhard Schmidt (Deutsches Elektronen-Synchrotron, Hamburg)

Vorgelegt dem Fachbereich Physik am 28. März 2012.

Deutscher Titel:
Elektro-optische Abtastung von THz-Strahlungspulsen an der kohärenten Übergangsstrahlungsquelle am FLASH-Beschleuniger

Steffen Wunderlich
Institut für Experimentalphysik
Universität Hamburg
Notkestraße 85
22607 Hamburg
steffen.wunderlich@desy.de

Diese Arbeit wurde mit LaTeX und dem KOMA-Script unter Verwendung der Farbpalette des TangoDesktopProject gesetzt.

Erklärung zur Eigenständigkeit

Hiermit versichere ich, dass ich die vorliegende Diplomarbeit selbstständig verfasst habe und – einschließlich beigefügter Abbildungen, Skizzen und Diagramme – keine anderen als die im Literaturverzeichnis angegebenen Quellen, Darstellungen und Hilfsmittel benutzt habe. Mit der Veröffentlichung meiner Arbeit erkläre ich mich einverstanden.

Steffen Wunderlich; Hamburg, den 28. März 2012

Abstract

Several applications in material science, non-linear optics and solid-state physics require short pulses with a high pulse energy of radiation in the far-infrared and in the terahertz (THz) regime in particular. As described in the following, coherent transition radiation generated by high-relativistic electron bunches at FLASH provides broadband single-cycle pulses of sub-picosecond length. The pulses are characterized using the quantitative and time-resolved technique of electro-optic sampling showing peak field strengths in the order of 1 MV/cm.

Zusammenfassung

Vielfältige Anwendungen in der Materialforschung, nicht-linearen Optik und Festkörperphysik erfordern kurze und hochenergetische Strahlungspulse im Ferninfraroten mit Frequenzen im Bereich um ein Terahertz. Wie nachfolgend beschrieben, bietet kohärente Übergangsstrahlung erzeugt von hochrelativistischen Elektronenpaketen am FLASH-Beschleuniger Strahlungspulse mit Längen unter einer Pikosekunde. Die Pulse werden mit der Technik der elektro-optischen Abtastung mittels eines zum Beschleuniger synchronisierten Lasersystems charakterisiert. Diese zeitaufgelöste und quantitative Methode zeigt Spitzenfeldstärken in der Größenordung von einem Megavolt pro Zentimeter.

Contents

List of Figures

List of Tables

Introduction

Terahertz radiation sources, in particular pulsed sources, are more and more requested for experiments in material science, non-linear optics and solid-state physics. For various applications on these fields, short pulses providing a high bandwidth and high focusability for maximum electric field strengths are required.
Laser-driven sources of THz pulses like photoconductive switches and the process of optical rectification in non-linear crystals deliver pulses with field strength in the order of 0.1 MV/cm at pulse energies of a few tens of microjoules, but of lengths of several picoseconds.
Coherent transition radiation (CTR) sources driven by electron accelerators allow experiments requiring MV/cm electric field strengths and short pulses. Since the spectrum of coherent transition radiation depend on the longitudinal and transversal electron bunch shape, such kind of sources also enable an approach for bunch diagnostics which is essential for the operation of a free-electron laser [WSB+11].
Detection schemes using the electro-optic effect enable a quantitative detection of THz pulses with sub-picosecond resolution in complex single-shot techniques, e.g. electro-optic spectral decoding [Ste07] and in the well controlled multi-shot technique of electro-optic sampling [WZ96].
This thesis describes the characterization of THz pulses at the coherent transition radiation source at the accelerator facility FLASH in Hamburg, which provides field strengths of 1 MV/cm [HSW+11]. The technique of electro-optic sampling is used to characterize the THz pulses in the time domain.
This document gives a short overview on the FLASH facility followed by an introduction into THz sources and the electro-optic detection in chapters 1 – 4. Then, the experimental setup at the accelerator and the laser laboratory are explained (chapter 5), before the results of the setup characterization and sampled THz pulses are presented and discussed in chapter 6.
The motivation of this work is the characterization of the CTR source for upcoming experiments requiring the pulse properties presented in the following.

1. The accelerator facility FLASH

The accelerator facility FLASH (**F**ree-electron **LAS**er in **H**amburg) is located at the research facility DESY in Hamburg, Germany.
Beginning in 1995, the free-electron laser (FEL) facility arose from the test facility for the TESLA linear collider project with integrated X-ray FEL [Sch10], which partly emerged in the International Linear Collider (ILC) project. The test facility has been upgraded several times for a user facility with improved electron energy, diagnostic elements and undulators [Sch10, SFF+10]. Today, the facility provides with electron energies up to 1.2 GeV photon wavelengths down to 4.45 nm generated in the SASE (self-amplification by stimulated emission) process [SFF+10, SDR08]. A seeding experiment is conducted presently [BAC+10].
FLASH consists of a laser-driven radio-frequency photoinjector gun, two bunch compressors (BC), seven superconducting accelerating structures (ACC) and several diagnostic tools which are described in this chapter.

Accelerating structures

Each of the seven accelerating modules consist of eight superconducting nine-cell resonator arrays shown in fig. 1.2 originally designed for the TESLA linear collider. Cooled to 2 K, each of the nine–cell arrays provide electric field gradients of up to 25 MV/m [ABB+00]. The standing-wave resonators have a fundamental frequency of 1.3 GHz and a quality factor $Q \approx 1 \cdot 10^9$. The RF power generated by klystrons is transported via non-evacuated copper waveguides and transmitted through ceramic

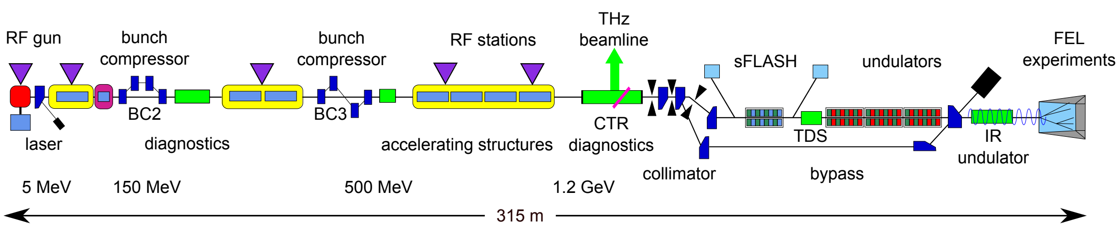

Figure 1.1.: Overview of the FLASH facility (not to scale). Adapted from [SFF+10].

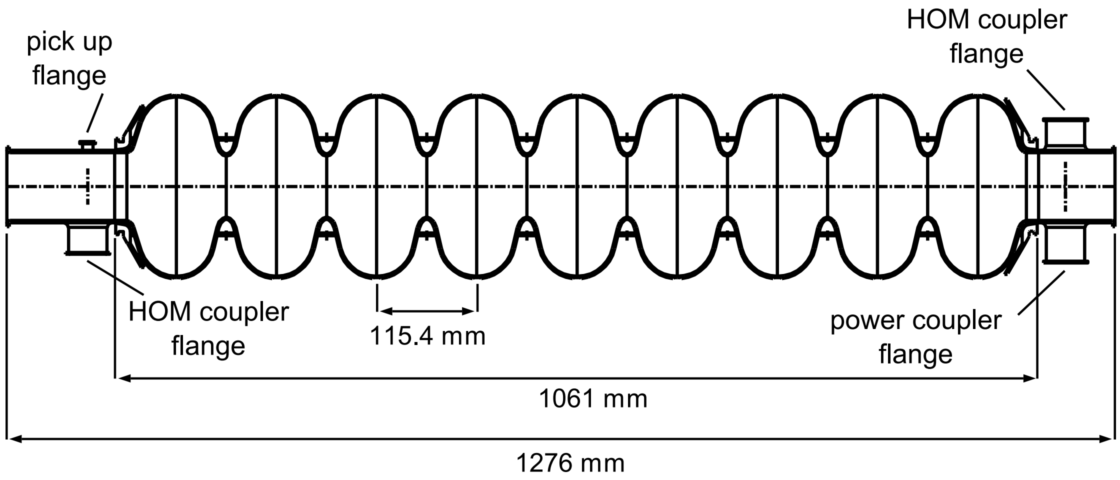

Figure 1.2.: Array of nine cavities made of solid niobium designed for a resonance frequency of 1.3 GHz [ABB+00].

windows into the cold and evacuated resonator arrays [ABB+00]. Due to the wake fields driven by the electron beam passing through the accelerating structures, higher order mode (HOM) couplers suppress the parasitic modes without extracting the fundamental frequency for acceleration.
Even though the superconducting accelerating modules enable a continuous wave (cw) operation at a reduced gradient, a pulsed operation scheme is used at FLASH [Sch10]. For normal operation, the resonator cavities are loaded with RF pulses with a flat top of 800 μs and referring to the timing scheme shown in fig. 1.3, this loading allows the acceleration of a bunch train every 10 Hz consisting of up to 800 bunches within 1 MHz repetition rate.

Bunch compression

At FLASH, two magnetic chicanes operating at electron energies of 150 MeV and 500 MeV, respectively are inserted to compress the electron bunches longitudinally [Stu04]. Regarding fig. 1.4, the compression depends on the acceleration in ACC1 and the third-harmonic RF structure ACC39 [EBH10] – in particular on the phase position of the electron bunch in the accelerating field.
Accelerating the particles in the bunch at the maximum of the sinusoidal accelerating field in the standing-wave resonators, a maximum energy gain is achieved. In the so-called ON-CREST operation, a dependancy energy – longitudinal position (energy chirp) is small. Shifting the RF phase to an electron position OFF-CREST, the energy

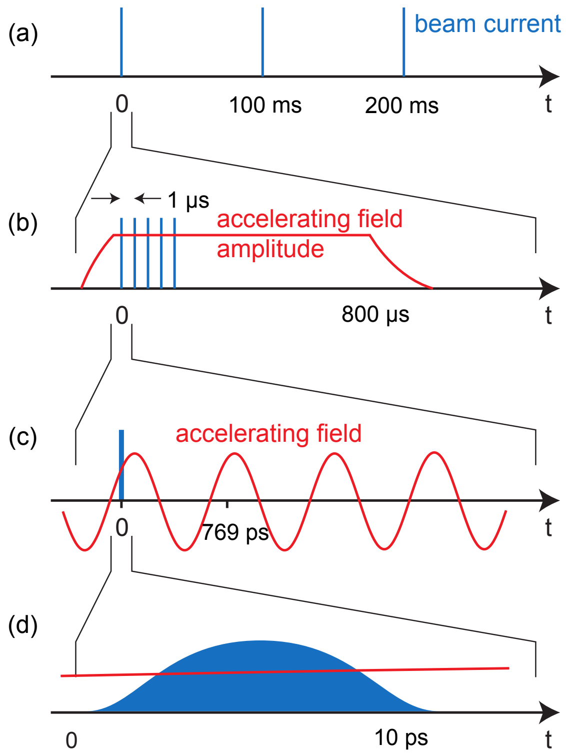

Figure 1.3.: Timing scheme used at FLASH (not to scale). (*a*) Bunch trains at 10 Hz repetition rate. (*b*) Amplitude of the accelerating field with a flat top of 800 μs. (*c*) The field at the fundamental frequency of 1.3 GHz with a period of approx. 769 ps accelerates a single electron bunch. (*d*) A single bunch of electrons of 10 ps length at the first accelerating module. Adapted from [Isc03].

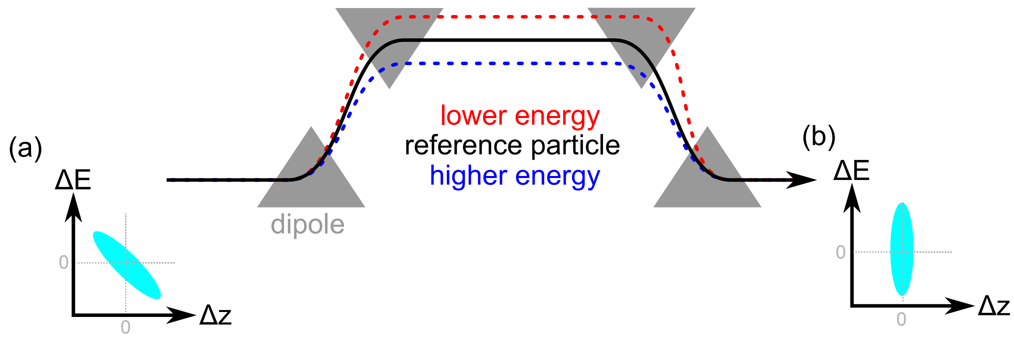

Figure 1.4.: Simplified scheme of a magnetic chicane for compressing an electron bunch coming from the left. The plots indicate the longitudinal phase space with respect to a reference particle. An energy – position dependancy (energy chirp) is introduced passing through ACC1. (*a*) The bunch with an energy chirp enters the magnetic chicane. (*c*) After the chicane, the phase space ellipse is set upright and the particle distribution is compressed. See text for details. Adapted from [Win08].

gain of an electron is now monotonously depending on the longitudinal position in the bunch. With an energy chirp introduced in ACC1, the deflection angle imprinted by the dipole magnets in the chicane acting on the electrons depends on the particle momentum. Electrons with higher momenta located in the tail of the bunch pass a shorter distance in the chicane due to the weaker deflection by the dipole magnets. After the passage through the bunch compressor, these electrons are shifted towards the head of the bunch and a longitudinal compression can be achieved.
The process of compression is monitored by bunch compression monitors (BCM) introduced in section 2. Typical bunch lengths achieved at FLASH at optimal compression are below 100 fs [BGG+12].

Longitudinal bunch diagnostics

In the SASE process [SDR08], electron bunches with high peak currents are required. Hence, diagnostics and control of the longitudinal bunch shape is necessary.
FLASH provides several instruments for longitudinal bunch diagnostics. Downstream of BC2 an electro-optic bunch length monitor [Bre11, Wiß12] and furthermore, behind the last accelerating module ACC7, a coherent transition radiation (CTR) station and transfer line [CSS+09, Wes12] and an electro-optic experiment for longitudinal

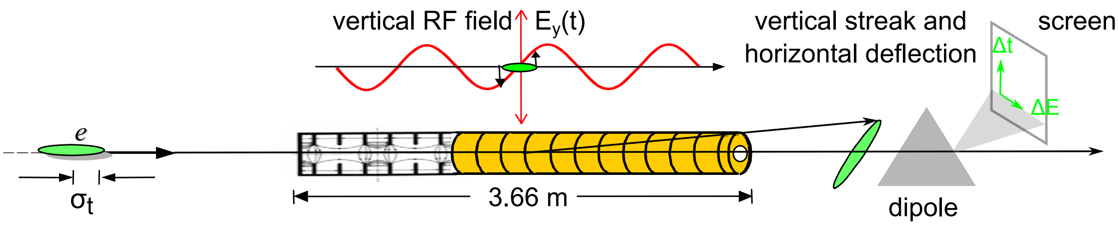

Figure 1.5.: Schematic of the transverse deflecting structure. An electron bunch is streaked by a transverse electric field in the RF cavities. In combination with an energy spectrometer consisting of a dipole magnet and a screen, both the longitudinal bunch shape and phase space can be investigated. Not to scale. Adapted from [Ste07].

diagnostics [Ste07, Wiß12] are installed. In front of the undulators, the transverse deflecting structure (TDS) based on LOLA-type cavities developed at SLAC [Sch06, ALL64] is located – fig. 1.5.
The principle of operation of the electro-optic bunch length monitor behind the first bunch compressor BC2, the electro-optic experiments behind ACC7 and in particular the CTR source and transfer line are treated in detail in this thesis.

SASE undulators

The free-electron laser facility produces light pulses in the SASE (self-amplified spontaneous emission) process, which starts from the spontaneous undulator radiation [SDR08].
The spontaneous undulator radiation is generated by the electron motion in the alternating magnetic field in the undulators. The wavelength λ of the emitted radiation seen under an angle θ with respect to the electron beam depends on the relativistic factor γ and the undulator parameter K representing the undulator properties of gap size, magnetic field strength B at the electron trajectory and magnetic period length λ_u.

$$\lambda = \frac{\lambda_u}{2\gamma^2}\left(1 + \frac{K^2}{2} + \gamma^2\theta^2\right) \text{ with } K = \frac{eB\lambda_u}{2\pi m_e c} \qquad (1.1)$$

The FEL process leads to an energy transfer from the electron beam to the light wave indicated in fig. 1.6. The condition for a constant energy transfer regarding a single electron is given by formula 1.1 at $\theta = 0$. To achieve a coherent superposition of many electrons in the bunch, the bunch has to be comparable or shorter than the emitted

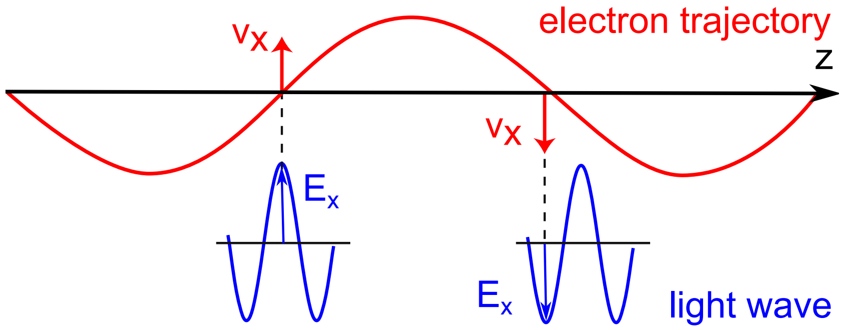

Figure 1.6.: Principle of the energy transfer from the electron beam (*red*) to the light wave (*blue*) due to the sinusoidal motion in the undulators. Taken from [SDR08].

light wave. A longitudinal arrangement of the electrons to positions near the positions of the maximum energy transfer occurs during the FEL process (*microbunching*). For details, please refer [SDR08].
To reach the saturation regime in photon energy gain [SDR08], the undulator section at FLASH consists of six undulator modules of 4.5 m length providing a K-value of 1.23 with NdFeB permanent magnets delivering a peak magnetic field of 0.48 T [SFF$^+$10].

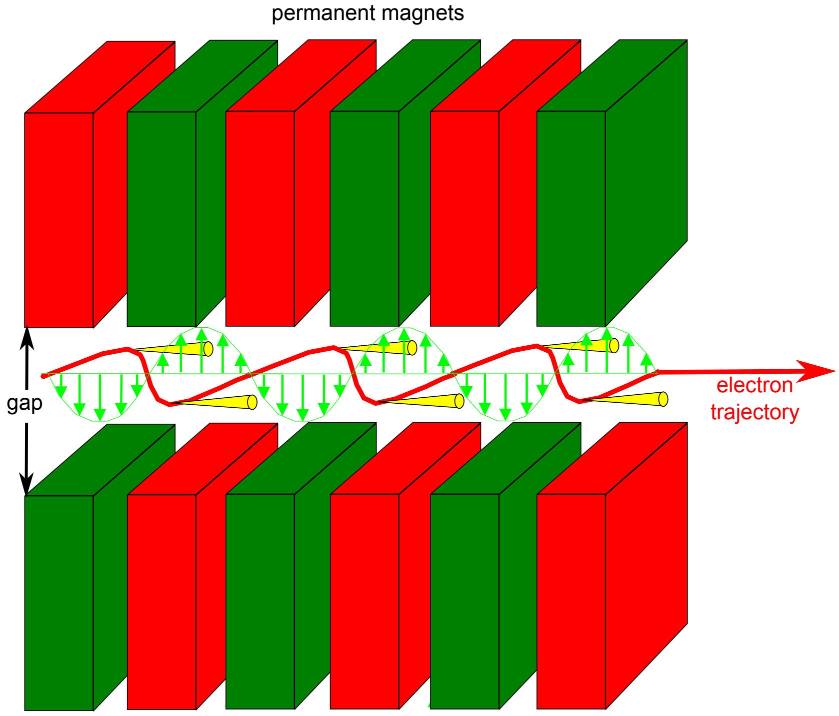

Figure 1.7.: Simplified schematic of an undulator with an electron beam (*red*), the magnetic field indicated in *green* and the radiation emitted (*yellow*). The electron oscillation is not to scale. Adapted from [FP99].

2. Diffraction and transition radiation based diagnostics at FLASH

In this chapter, the phenomena of diffraction radiation (DR) and transition radiation (TR) are introduced and their generation and application at FLASH are described. The operation of a free-electron laser requires a precise control of electron bunch parameters. The processes of DR and TR and in particular the coherent formation of DR and TR offer several approaches for transverse and longitudinal diagnostics of electron beam parameters like bunch compression, transverse and longitudinal bunch profiles.
The electric field of an electron in its rest frame A moving with $\beta = \frac{v}{c}$, a resting observer in the laboratory frame A' sees an electric field compressed in direction of propagation $\boldsymbol{z}$ parallel to $\boldsymbol{v}$ due to the Lorentz transformation.
The radial electric field of a point charge q seen by observer A' depending on the angle Ψ between $\boldsymbol{r}$ and $\boldsymbol{z}$ now becomes [Jac75]:

$$\boldsymbol{E}(r,t) = \frac{q}{4\pi\epsilon_0} \cdot \frac{1}{\gamma^2 \left(1 - \beta^2 \sin^2 \Psi\right)^{3/2}} \cdot \frac{\boldsymbol{r}}{r^3} \tag{2.1}$$

2.1. Diffraction radiation

Generation and properties

Diffraction radiation (DR) occurs when charged particles or an electron bunch in particular, passes through a slit, and hence, the electric field with a radial distribution given by formula 2.3 is deflected without intercepting the electrons motion. In a first approximation, the electric field of a charge distribution following a shape $Q(t)$ of an infinitesimal radius and of duration t_b is given by the convolution of equation 2.1 [Ste07]

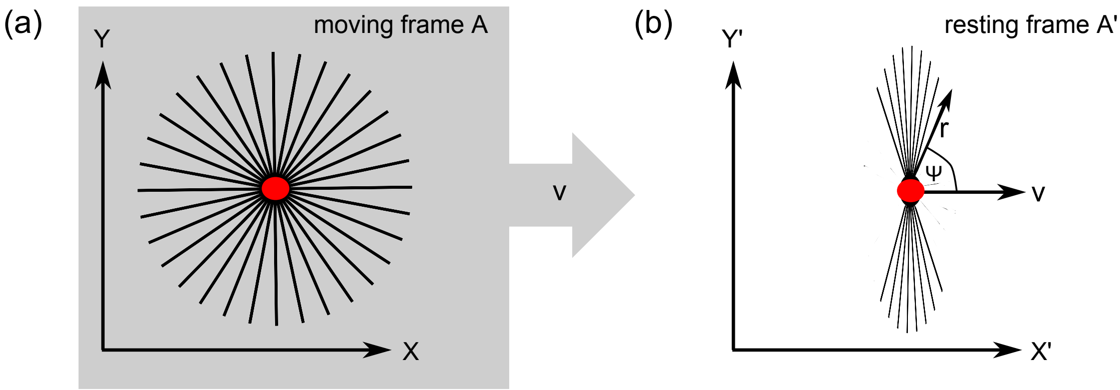

Figure 2.1.: (*a*) Electric field lines of an electron in its rest frame moving with v. (*b*) Field lines in the frame of a resting observer. Inspired by [Jac75].

$$Q(t) = \begin{cases} \text{const.} & [0, t_\text{b}] \\ 0 & \text{otherwise} \end{cases} \tag{2.2}$$

$$E_\text{r,bunch}(r,t) = \int_{-\infty}^{\infty} E_\text{r}(r, t-s)\, Q(t) ds \tag{2.3}$$

DR and, as introduced later, transition radiation (TR), can be described in the far field with the formula developed by GINZBURG and FRANK [CSS05]. The GINZBURG FRANK formula gives the spectral intensity per solid angle Ω of the source with an area element $dS = R\, d\Omega$ of the backward scattered radiation of an infinite screen of perfect reflectivity.

$$\frac{d^2 U_\text{GF}}{d\omega d\Omega} = \frac{e^2}{4\pi^3 \epsilon_0 c} \cdot \frac{\beta^2 \sin^2\Theta}{(1-\beta^2\cos^2\Theta)^2} \tag{2.4}$$

The radiation is observed under an angle Θ with respect to the electron trajectory – figure 2.2a. Regarding a finite and circular screen of radius a with a circular hole of radius b (fig. 2.2a, the formula (2.4) is corrected by terms $T_\text{a}(\Theta,\omega)$ and $T_\text{b}(\Theta,\omega)$ representing the source properties leading to oscillations in the angular distribution [CCOV99, CSS05].

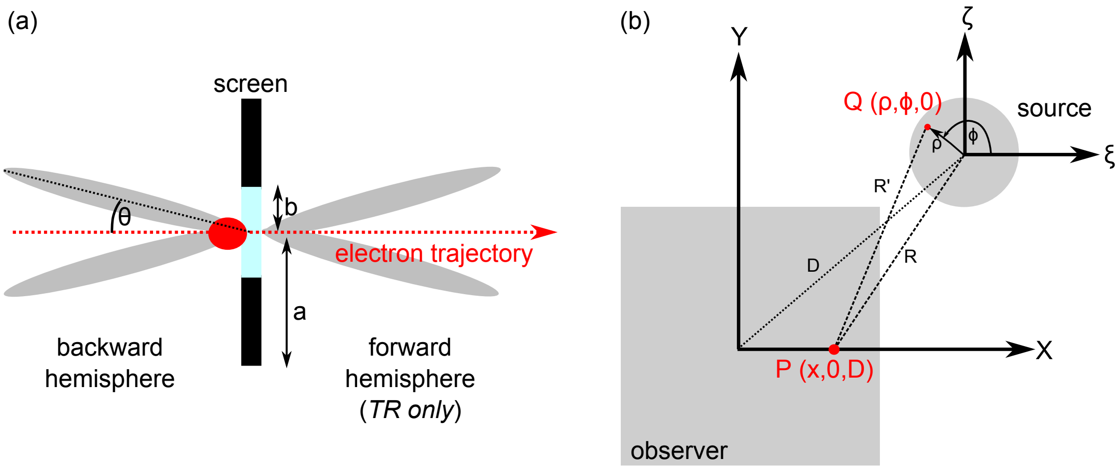

Figure 2.2.: (*a*) Screen as a source of diffraction radiation. For transition radiation, the screen provides no hole. (*b*) Geometry convention of a DR / TR source seen by an observing plane. See text for details.

$$\frac{d^2U}{d\omega d\Omega} = \frac{d^2U_{\text{GF}}}{d\omega d\Omega} \cdot \left[T_{\text{b}}(\Theta,\omega) - T_{\text{a}}(\Theta,\omega)\right] \tag{2.5}$$

In the case $b \to 0$ or $T_{\text{b}} \to 1$, transition radiation described in the next section occurs.
In the case of diffraction radiation, high frequency components are suppressed [CSS05].
The formulae (2.4) and (2.5) are valid in the far field regime, where the intensity distribution only depends on the distance R between the observer to the source and the FRAUNHOFER approximation for diffraction can be applied [Gob87].
In the near field, FRESNEL diffraction has to be applied and the intensity distribution also depends on the source on its plane indicated in fig. 2.2b. Details are treated in section 2.2.

2.2. Transition radiation

When electrons pass the boundary of two media with different dielectric constants, e.g. vacuum and solid matter, the conditions in the MAXWELL equations change rapidly and due to this change, radiation is emitted with properties depending on the incoming particle and the boundary [HSB91, TMKF92].

Generation and properties

The treatment of transition radiation (TR) is very similar to diffraction radiation. The consideration of a finite TR source, e.g. a dedicated TR screen of radius a yields a angular and spectral intensity distribution given by GINZBURG FRANK

$$\frac{d^2U}{d\omega d\Omega} = \frac{d^2U_{\mathrm{GF}}}{d\omega d\Omega} \cdot [1 - T_{\mathrm{a}}(\Theta, \omega)] \tag{2.6}$$

According to section 2.1, this formula is only valid in the far field. Indicated in fig. 2.2b, the distance R' of a point $P(x, 0, D)$ on an observing plane to a point on the source $Q(\rho, \phi, 0)$ has to be extended to the second order to consider $\rho \not\ll R$.

$$R' = \sqrt{D^2 + (x - \rho\cos\phi)^2 + (\rho\sin\phi)^2} \approx R - \frac{x\rho\cos\phi}{R} + \frac{\rho^2}{2R} \tag{2.7}$$

The near field approximation leads to a phase factor and with $k = \frac{\omega}{c}$ to an intensity distribution [CSS05] of

$$\frac{d^2U}{d\omega d\Omega} \propto \left| \int_0^a J_1(k\rho\sin\theta)\, K_1\left(\frac{k\rho}{\beta\gamma}\right)\, \exp\left(\frac{ik\rho^2}{2R}\right) \rho d\rho \right|^2 \tag{2.8}$$

with the Bessel function J_1 and the modified Bessel function K_1.
The near field approximation has to be taken into account, if the distance D between source and observer is smaller than the LORENTZ factor times the *effective source radius* $r_{\mathrm{eff}} = \gamma\frac{2\pi c}{\omega}$ [CCOV99]

$$D < \gamma r_{\mathrm{eff}} = \gamma^2 \frac{2\pi c}{\omega} \tag{2.9}$$

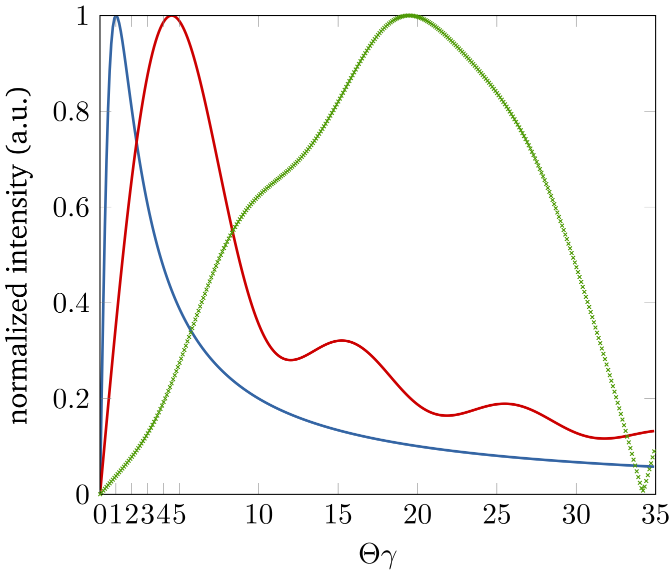

Figure 2.3.: Angular distribution of transition radiation by a circular disk for $f = 1$ THz and $\gamma = 1000$. (*Blue*) Following GINZBURG FRANK (2.4) with an infinite screen in the far field. (*Red*) Far field transition radiation by a screen of radius $a = 30$ mm following (2.6). (*Green*) Numerical solution of eqn. (2.8) for the near field. The far field condition (2.9) is not fulfilled in the distance of $D = 0.52$ m, which is position of the first optical element of the transfer line described section 5.2. Traces are individually normalized.

For typical values at FLASH, $\gamma = 1000$ and bunch lengths below 300 μm, the far field is reached in a distance of $D = 300$ m. This leads to a much wider angular distribution indicated by the green curve in fig. 2.3, which also has to be taken into account for the design of a transfer line for TR mentioned in section 5.2.

2.3. Coherent diffraction and transition radiation

If the electron bunch length becomes comparable or shorter than the wavelength of the emitted radiation, the electrons radiate in phase or coherently, the spectral intensity now scales quadratically with the number of particles N in the bunch assuming an infinitesimal small transversal size.

$$\frac{d^2U}{d\omega d\Omega} = \left(\frac{d^2U}{d\omega d\Omega}\right)_{\text{one particle}} \cdot \left(N + N(N-1) \cdot \left|F_{\text{long}}(\lambda)\right|^2\right) \tag{2.10}$$

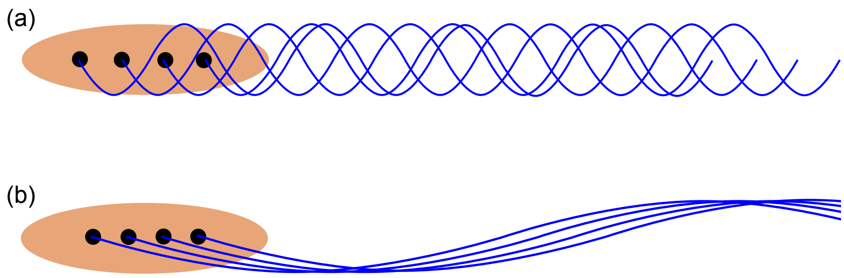

Figure 2.4.: (*a*) Mostly incoherent superposition of radiation components of single electrons in an electron bunch for wavelengths smaller than the bunch length. (*b*) For wavelengths larger than the bunch, a larger fraction of radiation components adds coherently. Inspired by [Beh08].

The longitudinal form factor $F_{\text{long}}(\lambda)$ is the Fourier transform of the line charge density $S(z)$ of the electron bunch propagating in z [Wes08, CSS05].

$$F_{\text{long}}(\lambda) = \int S(z)\, e^{-2\pi \frac{i\,z}{\lambda}}\, dz \tag{2.11}$$

A coherent superposition also occurs if the electron bunch provides a substructure. In consequence, the spectrum of coherent radiation includes higher frequencies corresponding to the length scale of this substructure. Typical bunch length at FLASH are below 100 fs (rms) [BGG+12], which corresponds to CTR frequencies above 10 THz.

Bunch compression monitors (BCM) at FLASH

Diffraction radiation is used for monitoring the longitudinal compression of the electron bunch in the two magnetic chicanes BC2 and BC3. The radiation generated at a rectangular slit is focused onto pyroelectric detectors [Wes12, BSWN10]. Depending on the compression introduced in the magnetic chicanes due to the energy chirp of the bunch, the coherent fraction of the diffraction radiation varies. Since the intensity of coherent DR increases for higher compression and shorter wavelengths [CSS05], the signal of the pyroelectric element [Beh08] carries the information of the bunch length and thus, of the compression state. In addition, the signal of the pyroelectric detector setup also depends on the beam position passing through the slit. In consequence, the bunch compression monitors at BC2 and BC3 are used to stabilize the phases of the accelerating modules ACC1 and ACC23 respectively, in a feedback system [Beh10].

Longitudinal bunch diagnostics

At relativistic energies, the electric field of an electron is longitudinally compressed. Regarding an electron bunch with a line charge density $S(z)$, most of the information of its electric field is located in the transverse plane. Besides acquiring the spectral intensity with e.g. spectroscopic methods [WSB+11], the phase information has to be obtained regarding the KRAMERS-KRONIG relation [LS97]. With this approach, the longitudinal bunch profile can be calculated following equation 2.11. A CTR spectrometer has been recently developed at FLASH delivering results in impressive agreement with measurements of the transverse deflecting structure [WSB+11, Wes12].

3. Terahertz radiation

Since the electric field of a relativistic electron bunch is longitudinally compressed and provides frequencies in the terahertz regime for FLASH parameters (see chapter 2), this chapter gives an overview of radiation in the frequency regime between 10^{11} to 10^{13} Hz – the terahertz (THz) frequencies. Beyond of general properties of this radiation, sources driven by laser systems and by electron accelerators are introduced. Then, selected applications and experiments with focus on THz pump / THz probe experiments are depicted. In the electro-magnetic spectrum, the THz regime is situated between the electronic frequencies up to a few gigahertz and the frequencies of the visible light beginning in the near-infrared of about 375 terahertz equaling a wavelength of approx. 800 nm.

3.1. Generation

As mentioned before, sources of terahertz radiation are located between electronic devices like Gunn-diodes and frequency multipliers [SR10] for frequencies up to several GHz. The frequencies in the infrared are generated by quantum-cascade lasers [LC00] or conventional laser systems like Yb-doped fiber lasers [LIW03] or titanium-sapphire oscillators [Mou82, Mou86]. Due to the progress in high-power laser systems and electron accelerators within the last twenty years [SR10], THz sources providing short and high-bandwidth pulses got available. In the following, the fundamental principle of operation and performance characteristics of the most important THz sources are introduced. A comprehensive treatment of terahertz radiation can be found in [SR10] and [CJW$^+$04].

The key performance characteristics of the sources mentioned in this chapter are compared in table 3.1

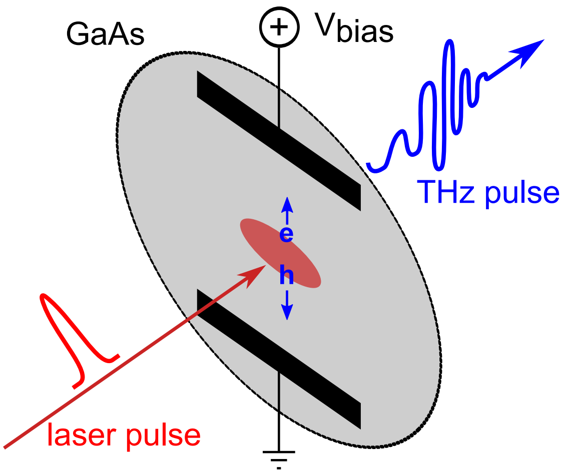

Figure 3.1.: Schematic of a photoconductive switch. Not to scale.

3.1.1. Laser-driven sources

Photoconductive switches

Introduced by Auston in 1983 [AS83b], photoconductive switches are the most common technique for both generation and detection of THz radiation. Photoconductive switches consist of a wafer of a semiconductor like gallium arsenide (GaAs) or indium gallium arsenide (InGaAs) grown by molecular beam epitaxy (MBE) [HF11]. On this wafer, a DC bias voltage of several kV/cm is applied and when a femtosecond laser pulse hit this wafer, electron-hole pairs are generated. The free charge carriers are immediately accelerated by the bias field and the resulting fast change in polarization drives the emission of pulses in the order of one picosecond and with frequencies in the THz regime.

With incident laser pulses of < 50 fs width and 4 μJ pulse energy, THz pulses of 36 kV/cm field strengths and pulse energies of 6 nJ have been reported [BSK$^+$10]. Furthermore, photoconductive switches can be used for detection of THz radiation. Here, no bias voltage is applied. The free charge carriers generated by incident laser pulses are accelerated by the electric field of the THz radiation and the current between the two bias electrodes allows to measure the electric field strength of the THz field [AS83b, HF11].

Process of optical rectification

The second laser-based process for generation of THz radiation mentioned here is optical rectification (OR) with a first experiment reported in 1962 [BFWW62]. Here, an ultrashort and intense laser pulse passes through a non-linear crystal like lithium niobate ($LiNbO_3$) or zinc telluride (ZnTe). Based on the interaction of the frequency components of the laser pulse over the length of the crystal (intrapulse DFG) [GTKC70, HF11], an electro-magnetic wave builds up and with short and broadband laser pulses, broadband THz pulses can be produced.
By layering of materials with an $\chi^{(2)}$ alternating in sign in particular (please refer to chapter 4), the generation of narrow band THz pulses has been reported [Vod06].

3.1.2. Electron accelerator-driven sources

Undulator radiation

As introduced in chapter 1, in the sinusoidal motion in an alternating magnetic field of an undulator (fig. 1.7 on page 7), the electrons emit radiation with wavelengths depending on the relativistic factor γ and the undulator properties given by eqn. (1.1). Due to this, undulator radiation provides a narrow bandwidth of

$$\frac{\Delta\lambda}{\lambda} \propto \frac{1}{N \cdot n} \tag{3.1}$$

with harmonic number n and undulator periods N [Cla04].
At FLASH, behind the SASE undulators, a dedicated undulator based on electromagnets produces far-infrared radiation originally used for bunch diagnostics [Wil08]. Performance data are also given in table 3.1.

Free-electron laser

Besides undulator radiation as phenomenon itself, the process of coherent superposition of the undulator radiation in the free-electron laser (FEL) process allows to achieve high-power pulses at wavelengths down to the X-ray regime [SDR08].
Low-gain free-electron laser consist of one or more undulators, where an electron beam accelerated by a linear accelerator or a storage ring emits undulator radiation, which is captured in an optical cavity made of mirrors and is amplified in each cycle.

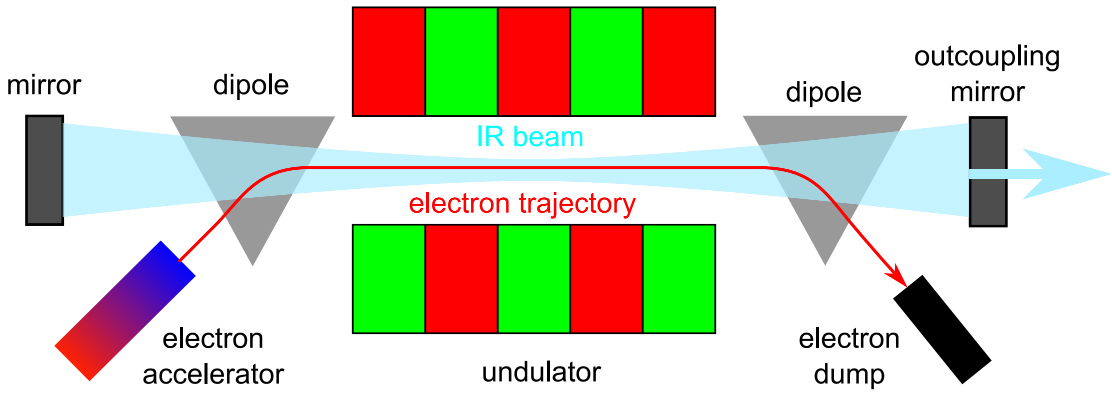

Figure 3.2.: Schematic of a low-gain free-electron laser. The light (*blue*) emitted by the electron beam (*red*) is captured and amplified in each cycle.

Due to the limited reflectivity of mirrors in the ultraviolet regime, low-gain FELs are only usable for the wavelength range of the visible and infrared light. The facilities FELBE at Rossendorf near Dresden, Germany [MGG+04] and FELIX near Utrecht, The Netherlands [Van04] provide sub-picosecond pulses at wavelengths between 5 and 250 μm with pulse energy of up to 50 μJ. The FEL facility at Novosibirsk, Russia delivers pulses with wavelengths in the range of 120 and 230 μm and energies of 40 μJ [VGK+06].

Wavelengths below of 140 nm in the vacuum-ultraviolet (VUV) and X-ray regime are produced by *high-gain* FELs, where the energy transfer from the electron beam to the light wave due to the motion in the undulators is carried out in a single pass trough many undulator periods. The energy gain is limited by the charge density modulation on the electron bunch imprinted by the energy transfer [SDR08].

Diffraction and transition radiation

As introduced in chapter 2, coherent transition radiation (CTR) generated by ultra-relativistic electrons at linear accelerators provides frequencies in the THz regime.

At CTR sources at the Linac Coherent Light Source (LCLS) at the Stanford Linear Accelerator Center (SLAC) CA, USA [DGF+11] and at FLASH, single-cycle THz pulses exceeding 1 MV/cm have been achieved [HSW+11]. In particular, those radiation sources provide short pulses and thus a large bandwidth required for various experiments introduced in the next section.

Table 3.1.: Overview of performance characteristics of THz sources. See text for details.

	Photoconductive switches	Optical rectification	Undulator radiation	FEL	CTR
Electric field [kV/cm]	36	1000	500	n/a	> 1000
Pulse energy [μJ]	$6 \cdot 10^{-3}$	3	2	50	140
Ref.	[BSK+10]	[HDBT11]	[FWG+09]	[Van04]	[DGF+11]

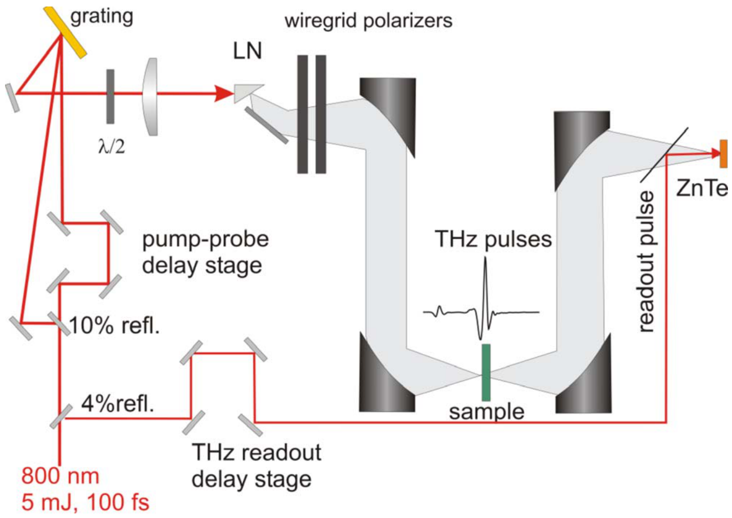

Figure 3.3.: A THz pump THz probe experiment for the investigation of charge carriers in semiconductors [HHH+09]. A laser system generates both the pump and probe beam by optical rectification in lithium niobate (LN). In addition, a small fraction of the laser power is used for THz detection by electro-optic sampling described in this thesis.

3.2. Selected applications and experiments

Pulses providing frequencies in the terahertz regime are of interest also beyond accelerator physics. Due to the low photon energies of a few millielectronvolts, THz radiation enables non-destructive investigation of e.g. semiconductors, of charge carriers or impurities in particular. The striking advantage of the availability of short THz pulses is the time-resolved technique of THz pump / THz probe schemes [HHH+09].

In the experiment depicted in figure 3.3, both the THz pump and THz probe beams are generated by optical rectification. Using a mechanical delay stage, the beams are delayed to each other enabling the investigation of the response in time of scattered

charge carriers in GaAs and InSb [HHH+09].
Another application of terahertz radiation is the characterization of XUV pulses generated by a SASE FEL using streaking techniques [Frü09, FWG+09]. The photoelectrons generated by the exposure of a noble gas by a XUV pulse are streaked by a terahertz pulse of a few picoseconds length. The energy of the photoelectrons now depends on the phase position in the ponderomotive potential of the terahertz field.
In solid-state physics, recent works report the characterization of superconductivity in cuprates with terahertz radiation [FTD+11]. Here, $\mathrm{LESCO}_{1/8}$, a normal conducting stripe-ordered compound of cuprate, is pumped by mid-infrared light and thus, superconductivity is induced. Acquiring the reflectivity of terahertz radiation allows to characterize the photoinduced state of superconductivity.

4. Electro-optic detection

The electro-optic (EO) effect in optically active crystals offers a quantitative method to determine the electric field of external radiation pulses in the THz regime. In combination with several detection schemes described in this chapter, the shape of the THz pulses can be obtained in the time-domain in single- and multi-shot techniques of different complexity.

4.1. The electro-optic effect

When an electric field e.g. of a THz pulse is applied to an optically active crystal, the polarization $\boldsymbol{P}$ of the crystal becomes dependent on the external electric field $\boldsymbol{E}_{\mathrm{THz}}$. The electric susceptibility tensor χ_e in the electric displacement $\boldsymbol{D}$ [Gri99]

$$\begin{aligned} \boldsymbol{D} &= \epsilon_0 \boldsymbol{E}_{\mathrm{THz}} + \boldsymbol{P} \\ &= \epsilon_0 \left(1 + \chi_e\right) \boldsymbol{E}_{\mathrm{THz}} \end{aligned} \tag{4.1}$$

gives the constant of proportionality in the polarization depending on the electric field. For high field strengths, higher orders have to be taken into account and thus, the Taylor expansion of the polarization yields in general

$$\begin{aligned} \boldsymbol{P} &= \epsilon_0 \chi_e \boldsymbol{E}_{\mathrm{THz}} \\ &= \epsilon_0 \left(\chi_e^{(1)} \boldsymbol{E}_{\mathrm{THz}} + \chi_e^{(2)} \boldsymbol{E}_{\mathrm{THz}}^2 + \chi_e^{(3)} \boldsymbol{E}_{\mathrm{THz}}^3 + \dots\right) \end{aligned} \tag{4.2}$$

where the occurrence of the effects in $\boldsymbol{E}_{\mathrm{THz}}$, ${\boldsymbol{E}_{\mathrm{THz}}}^2$ and ${\boldsymbol{E}_{\mathrm{THz}}}^3$ depends on the crystal. Here, only the term of $\chi_e^{(2)}$ giving the linear dependance of the refractive index on the electric field, i.e. the *linear Pockels effect*, is used for the determination of the electric field of THz pulses in gallium phosphide (GaP) and zinc telluride (ZnTe) [Ste07]. Without an external electric field, the refractive index is isotropic. Figure 4.1a shows

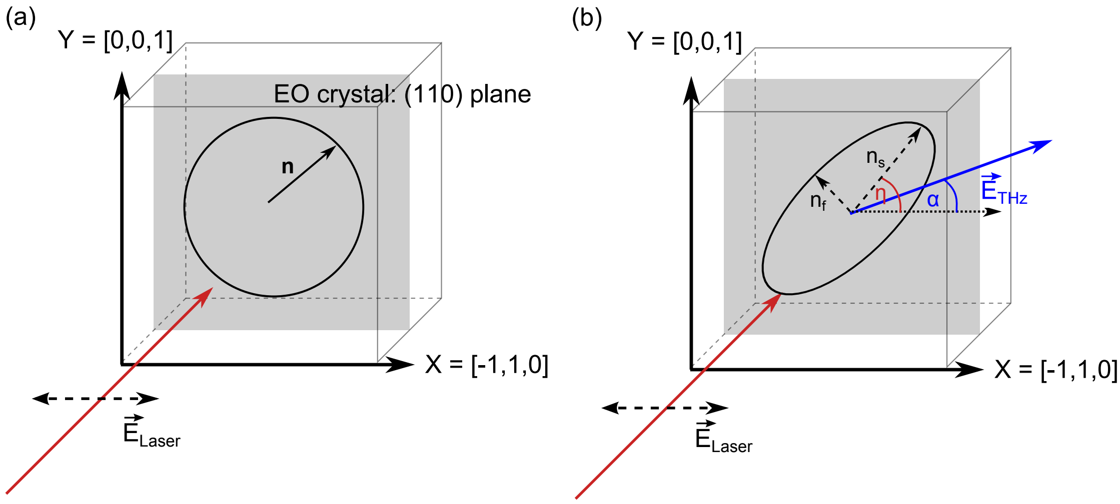

Figure 4.1.: The refractive index of an electro-optic crystal on the (110) plane. (a) Without an external electric field, the refractive index in non-birefringent crystals is isotropic. An incident linearly polarized laser does not experience a change in polarization. (b) The crystal becomes birefringent and thus, the laser becomes elliptically polarized. For an angle $\alpha = 0$ deg, the change in polarization is maximal. Adapted from [Ste07].

the crystal plane (110) defined by the axis $\boldsymbol{X}$ and $\boldsymbol{Y}$ and the refractive index in this plane.

In the presence of an external electric field $\boldsymbol{E}_{\mathrm{THz}}$ but independently from a read-out laser pulse, the refractive index becomes non-isotropic due to the change in polarization. This change depends on the angle α between the electric field vector $\boldsymbol{E}_{\mathrm{THz}}$ and the optically active axis $\boldsymbol{X}$. As depicted in fig. 4.1, the crystal plane (110) now provides two components in refractive index, a slow component of a larger refractive index n_{s} and a fast component n_{f}.

A linearly polarized laser pulse passing through the crystal experiences a phase retardation $\Gamma(\alpha)$ between the two orthogonal components of the laser polarization caused by the two different projections of the components in refractive index n_{s} and n_{f} on the laser polarization [Ste07, Bre11].

$$\Gamma(\alpha) = \frac{\pi\, d}{\lambda}\, n_0^3\, |\boldsymbol{E}_{\mathrm{THz}}|\, r_{41}\, t_{\mathrm{refl.}} \sqrt{1 + 3\cos^2(\alpha)} \tag{4.3}$$

with the non-modified refractive index n_0 seen by the laser of center wavelength λ, the linear electro-optic or Pockels coefficient r_{41} [Ste07], the crystal thickness d and

angle α between $\boldsymbol{E}_{\mathrm{THz}}$ and the optically active axis $\boldsymbol{X}$. The coefficient $t_{\mathrm{refl.}}$ describes the reflective losses at the crystal surface (FRESNEL equations) [HSW+11].
In addition, the orientation of the laser polarization to the refractive index ellipse is important. Regarding figure 4.1, the angle α between the THz field vector $\boldsymbol{E}_{\mathrm{THz}}$ defines the orientation of the index ellipse to the crystal axis. Introducing the angle η between the crystal axis $\boldsymbol{X}$ and the major axis of the ellipse indicated by n_{s}, the imprint of the phase retardation Γ on a linear polarized laser pulse depends on the angle η. A laser pulse linearly polarized parallel to the major or to the minor axis of the index ellipse experiences no phase retardation, which is the case at e.g. $\alpha = \pi/2$ [Ste07]. The plots in figure 4.2 illustrate the dependence of the orientation of the index ellipse to the $\boldsymbol{X}$ axis (*left*) and the phase retardation Γ (*right*) on angle α following equations (4.3) and (4.4).

$$\cos(2\eta) = \frac{\sin(\alpha)}{\sqrt{1 + 3\cos^2(\alpha)}} \tag{4.4}$$

For increasing electric field strength E_{THz}, the effect of *over-rotation* occurs [Ste07]. Regarding fig. 4.1, the refractive index ellipse turns by π with increasing phase retardation and in consequence, the acquired change in polarization turns the sign with rising field. To overcome this, thinner crystals or crystals providing a smaller Pockels coefficient r_{41} can be used. Decreasing the crystal thickness leads to a reduction of the imprint of the phase retardation on the laser pulse and in consequence to a lower signal to noise ratio.

4.2. Electro-optic crystals

Crystal structures with a lack of inversion symmetry provide a susceptibilty component $\chi_e^{(2)} \neq 0$ and thus, the linear electro-optic effect [Ste07] . Commonly used materials are gallium phosphide (GaP) and zinc telluride (ZnTe) with a zincblende crystal structure. All crystals used for this experiment are cut in the (110) plane and mounted in holders allowing a rotation around the axis perpendicular to the $\boldsymbol{X}$ and $\boldsymbol{Y}$ axis. A main property of interest is the refractive index in the infrared for the laser of 800 nm center wavelength and in the THz regime. To maintain the phase matching [Ste07] between the THz pulse and the laser pulse co-propagating through the crystal, the refractive indices have to be as close together as possible. The refractive indices and ZnTe and GaP are shown in figure 4.3 for wavelengths in the near-infrared and far-infrared. The

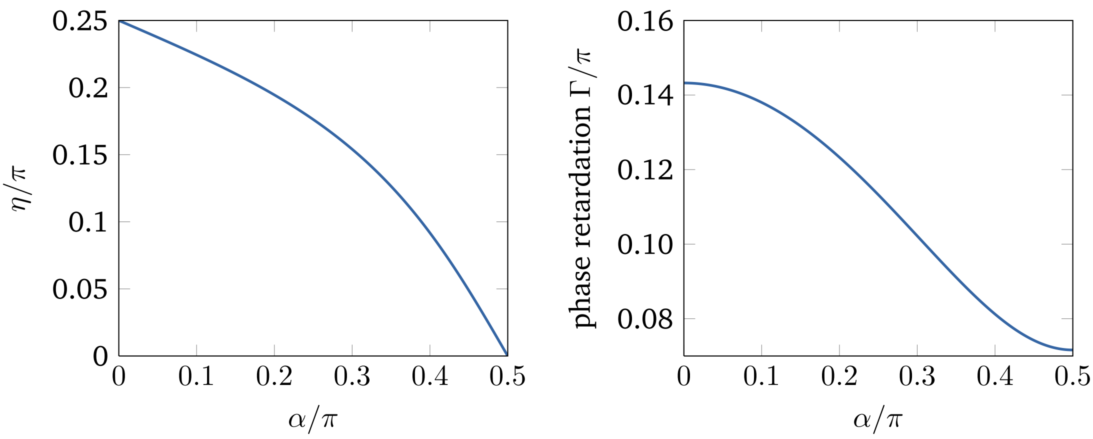

Figure 4.2.: (*Left*) Angle η between axis n_s and crystal axis $\boldsymbol{X}$ and (*right*) phase retardation both depending on angle α. Calculation for a GaP crystal of 200 µm thickness and $E_{\text{THz}} = 100$ kV/cm. Adapted from [Ste07].

curves are fits following [Ste07] based on experimental data taken by [AS83a] and [War91].

As depicted, ZnTe and GaP show a resonant behavior at frequencies of 5.3 THz and 11 THz, respectively. These resonances due to the excitation of transverse optical lattice oscillations [Ste07] limit the frequency range for detection of radiation with frequencies in the THz regime. In the experiment described in this thesis, only the frequency range below the resonances is taken into account [CSS+09].

The second important quantity is the Pockels coefficient r_{41}, which is frequency dependent and also shows the resonances mentioned above. The measurement of this quantity is complex [Ste07] but the values for ZnTe and GaP are almost constant for frequencies below the resonances:

$$\text{ZnTe: } r_{41} = 4.04 \cdot 10^{-12} \frac{\text{m}}{\text{V}} \text{ [PMR}^{+}\text{08]}$$
$$\text{GaP: } r_{41} = 0.88 \cdot 10^{-12} \frac{\text{m}}{\text{V}} \text{ [BMNC89]}$$

4.3. Detection techniques

Several techniques using the linear electro-optic effect exist for detection of THz radiation, including multi-shot schemes of good practicality and single-shot techniques

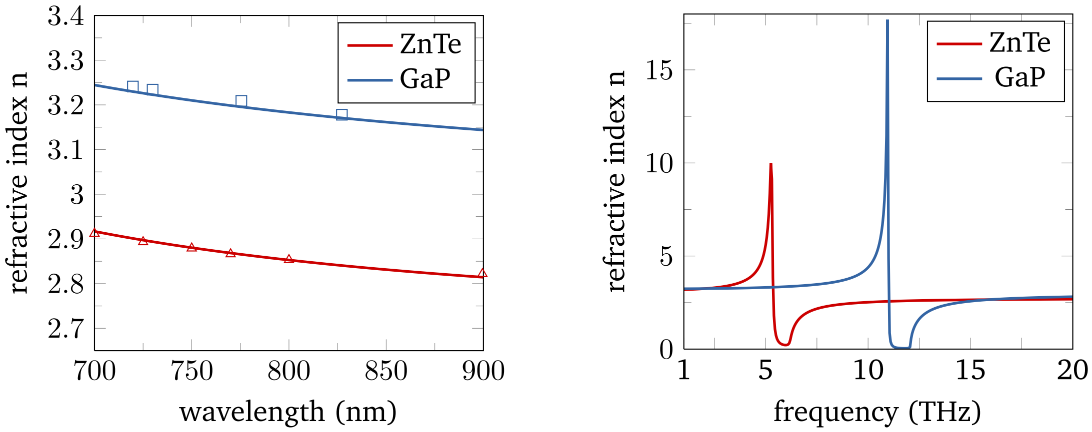

Figure 4.3.: Real part of the refractive indices of ZnTe and GaP in the near-infrared (*left*) and for THz frequencies (*right*). See text for details. Following [Ste07].

requiring more complex setups and laser pulse properties [Ste07].

Spectral decoding

One technique for single-shot detection of THz pulses of a few picoseconds length is *spectral decoding*. Here a laser pulse with a linear chirp [DR06] passes through the crystal collinear with the THz pulse. The temporal shape of the THz pulse propagating through the crystal is translated into a wavelength dependent change in polarization. Acquiring a reference spectrum without the THz field and spectra modified by the electro-optic effect in presence of the THz field allows to deduce the temporal shape of the THz pulse [Ste07, Bre11]. This scheme suffers from the problem of frequency mixing of spectral components of the laser pulse and the THz field. In addition, both the chirp and the overall length of the laser pulse limit the resolution of detection and the width of the time window.

Sampling

Due to the availability of THz sources, in particular electron accelerators providing a good shot-to-shot stability [Löh09], short laser pulses of some tens of femtoseconds can be used to sample the external electric field in time-domain using a scanning delay in a multi-shot measurement. Regarding the experimental setup, this scheme is the most simple technique [WZ96]. The polarization state of the laser pulses passing the scanning delay stage is set in the polarizer and while passing through the crystal in the

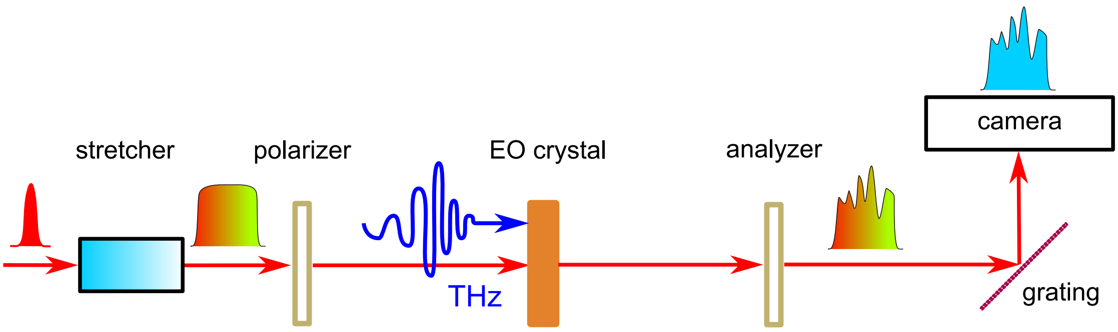

Figure 4.4.: Setup for electro-optic spectral decoding. The polarizer sets a linear state of polarization for the chirped laser pulse. Due to the phase retardation introduced in the presence of the THz field, the spectrum is modified. The temporal shape of the THz pulse is translated into a wavelength dependent change in polarization state detected by a spectrometer consisting of a reflective grating and a CCD camera. For details, see text. Adapted from [Ste07].

absence of an external electric field, the linear polarization state is not altered disregarding a residual birefringence of the EO crystal. After transformation of the linear polarization into circular polarization by a following $\lambda/4$ retarder, a Wollaston prism [Gob87] splits the laser pulses into two components with polarization parallel and perpendicular to the optical axis defined by the polarizer. Both of the two components have the same intensities I_1 and I_2 detected by photodetectors.

Applying a THz field on the crystal, the polarization gets slightly elliptical in linear dependence on the external electric field following formula (4.3). Hence, the intensities I_1 and I_2 of the two polarization components change depending on the phase retardation.

This specific method of signal detection is the *balanced detection* technique, which allows to cancel out amplitude jitter of the laser pulse intensity by acquiring and normalizing to the sum of the two photodetector signals. The phase retardation (4.3) acquired in the crystal now translates to the two photodetector signals I_1 and I_2 [Ste07]

$$
\begin{aligned}
\Gamma(\alpha) &= \frac{\pi\, d}{\lambda}\, n_0^3\, |\boldsymbol{E}_{\mathrm{THz}}|\, r_{41}\, t_{\mathrm{refl.}} \sqrt{1 + 3\cos^2(\alpha)} \\
&= \sin^{-1}\left(\frac{I_1 - I_2}{I_1 + I_2}\right)
\end{aligned}
\tag{4.5}
$$

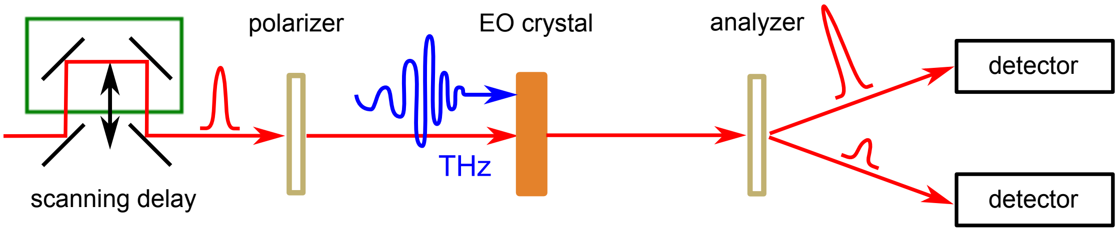

Figure 4.5.: Setup for electro-optic sampling using a scanning delay. The laser pulses of some tens of femtoseconds width pass through the scanning delay enabling a time-resolved acquisition of the electric field of the THz pulse over multiple shots. The analyzer consists of a retarder and a Wollaston beam-splitter. The photodetectors acquire the modulated intensities of the laser pulses depending on the phase retardation. See text for details.

The resolution in time is defined by the width of the laser pulses and the timing stability between the laser pulses and the THz pulses generated by the CTR source driven by an electron accelerator. The former can be determined by e.g. autocorrelation. The measurement and evaluation of the latter is more complex, please refer to chapter 6. A fundamental resolution limit is given by the crystal resonances introduced in section 4.2.

5. Experimental setup at FLASH

The characterization of THz pulses from the coherent transition radiation (CTR) source at FLASH requires a complex setup for the generation of the pulses, the transport into a laboratory outside the shielded accelerator area and the detection using a laser system. This chapter gives a short overview on the specific facilities, the experimental setup and the instruments used for this experiment.

5.1. CTR source

The screen station located at position "17ACC7" behind the last accelerating module provides several screen configurations beginning with *on-axis* screens for total interception of the electron beam and *off-axis* screens enabling a complementary operation during the FEL operation. All the screens are made of silicon with a thickness of 380 µm and are equipped with a 150 nm aluminum coating [HSW$^+$11].
The standard screen used for CTR generation is at the *off-axis* position 10 mm horizontally shifted from the electron trajectory and provides dimensions of $(15$ x $25)$ mm. A kicker magnet allows to deflect the last bunch of a bunch train onto the screen at a repetition rate of 10 Hz. The deflection angle is approx. 0.2 deg and the distance between kicker and screen is 3.6 m as depicted in fig. 5.1.

5.2. CTR transfer line

To guide the radiation generated at the screen located in the accelerator vacuum, a transfer line of a length of approx. 21 m is installed. This transfer line (fig. 5.2) images the screen into an external laser laboratory by focusing toroidal mirrors providing a gold coating. A wedge-shaped diamond window separates the accelerator vacuum with pressures in the order of 10^{-9} mbar from a secondary vacuum maintained in the transfer line until the laboratory. The diamond window chosen for a high transmission for far-infrared radiation has a thickness of 0.5 mm and a diameter of 20 mm. The

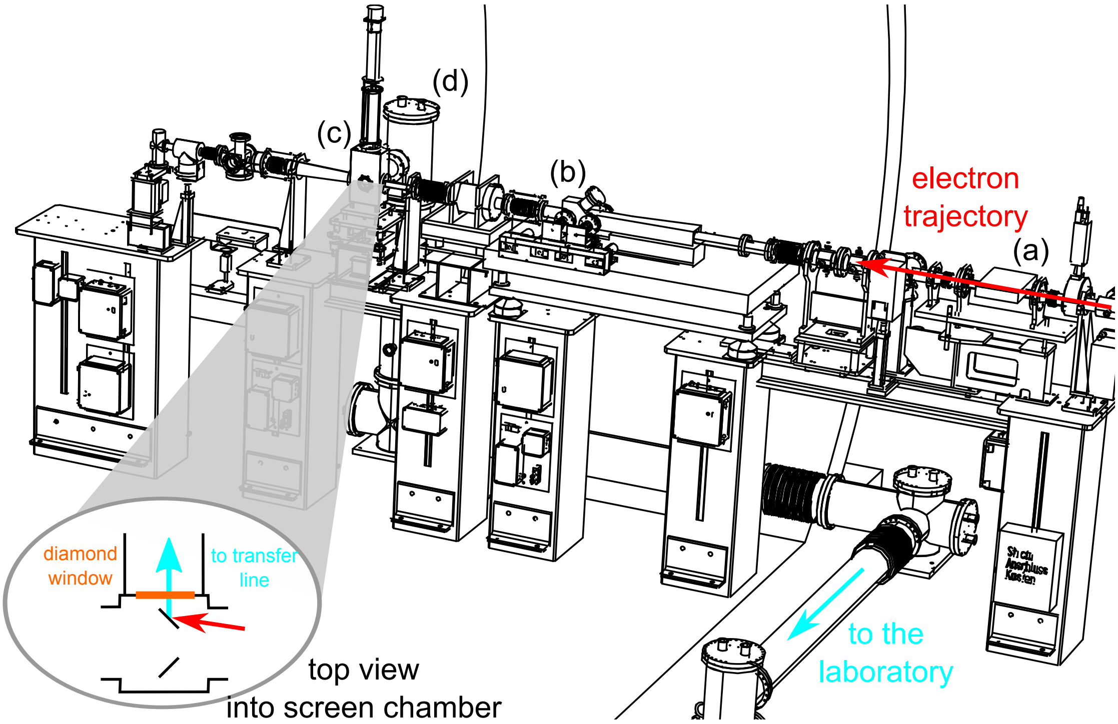

Figure 5.1.: Schematic of the setup at the accelerator electron beam line. The electron beam (*red*) is deflected by a kicker magnet (*a*) and hits the screen in the chamber (*c*) after passing through the chamber for EO experiments (*b*). The radiation is guided into a secondary vacuum and, beginning with the first focusing mirror at (*d*), transported into an external laboratory. The distance between the kicker and the screen is approx. 3.6 m. By courtesy of Kai Ludwig.

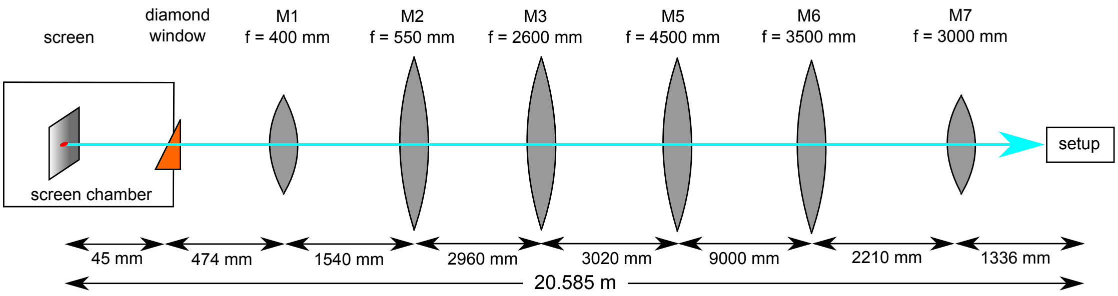

Figure 5.2.: Schematic of the transfer line providing focusing mirrors to image the screen into the external laboratory [CSS+09]. Data by courtesy of Kai Ludwig. Not to scale.

secondary vacuum pressure is kept at less than 0.1 mbar to decrease losses of the THz radiation in humid air [CSS+09, XAS+06].

5.3. Laser system

5.3.1. Titanium-sapphire oscillator

The system is a commercial MICRA-oscillator pumped by a VERDI-5 (cw) laser both manufactured by COHERENT INC., USA.
The titanium-sapphire oscillator delivers pulses at a center wavelength of 800 nm with a typical length of approx. 35 fs (please refer to measurements in section 6.1) at an average power of approx. 500 mW. At a repetition rate of 81 MHz, this corresponds to pulse energies of 6 nJ. The oscillator is based on passive mode-locking conducted by KERR lensing [DR06] in the titanium-sapphire crystal which is the lasing medium [Mou82, Mou86].

5.3.2. Synchronization

The laser oscillator is synchronized with the FLASH master oscillator which provides a radio-frequency signal of 1.3 GHz electrically distributed by coaxial lines along the accelerator facility [Win08]. The laser pulses with a repetition rate of approximately 81 MHz are exposed to a photodetector (EOT ET-4000F) with a bandwidth larger than 12 GHz. This photodetector signal also yields high harmonics of the laser repetition rate from which the 16th harmonic of about 1.3 GHz is used for synchronization.
The signal of the master oscillator and the laser are compared in a phase-lock loop

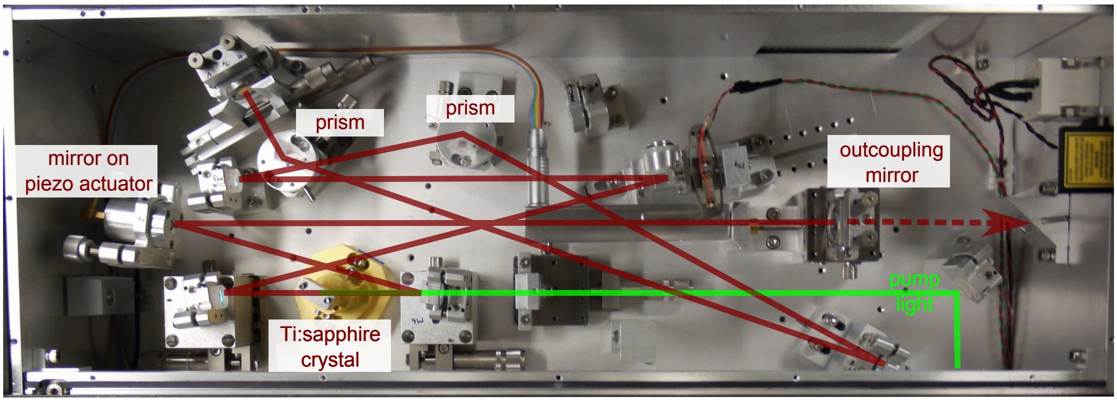

Figure 5.3.: Photograph of the laser cavity. The pump light (*green*) maintains the population inversion in the titanium-sapphire crystal. The generated pulsed beam (*red*) of a center wavelength of 800 nm oscillates in the cavity defined by the end mirrors. One of them provides a raised transmission and enables the extraction of laser pules used for the experiment.

(PLL) based on RF downmixing with the key component of a digital signal processing (DSP) unit. Fig. 5.4 shows a schematic of the PLL. The output of the mixer type MINI-CIRCUITS ZFM-2000+, i.e. the error signal S_{error}, represents the phase difference of the two signals S_{laser} and S_{RF} with phases ϕ_1 and ϕ_2 following equation (5.1), in which the term giving the frequency sum is canceled with a low-pass filter with a cutoff frequency of 1.9 MHz.

$$\begin{aligned} S_{\text{error}} = S_{\text{laser}} \cdot S_{\text{RF}} &\propto \sin(\phi_1 + \alpha) \cdot \sin(\phi_2) \\ &\propto \cos(\phi_1 - \phi_2 + \alpha) + \underbrace{\cos(\phi_1 + \phi_2 + \alpha)}_{\text{canceled}} \end{aligned} \tag{5.1}$$

The error signal is delivered via an analog-to-digital converter (ADC) to the DSP, which tunes the laser cavity in length by acting on a piezo actuator. The relative position of the laser pulse train with respect to the electron bunches can be changed by acting on the 1.3 GHz reference signal using a digitally controllable vector modulator (VM) [HSW+11].

Using the 1.3 GHz signal for high-accuracy locking, the position in phase at the fundamental frequency of the laser system at 81 MHz is not unequivocal - 16 zero crossings of the 1.3 GHz occur in one period of the lasers fundamental frequency. A second part of the loop operates at 81 MHz consisting of a phase detector

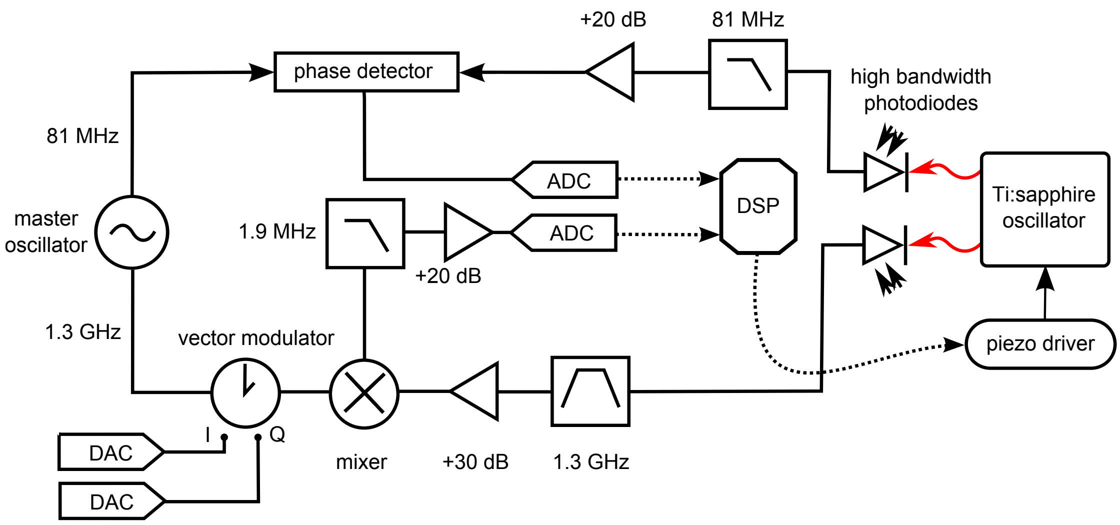

Figure 5.4.: Schematic of the phase-lock loop for synchronization of the laser system with the master oscillator of FLASH. Both the fundamental frequencies of the master oscillator and the laser system are used to maintain a timing uncertainty in the order of 100 fs [HSW+11].

(ANALOGDEVICES 8302) similar to the mixer of the 1.3 GHz loop. The signal of this phase detector is also processed by the DSP regulation, which maintains the phase position to the 81 MHz reference signal. The input signal for the second loop is generated by a photodetector type HAMAMATSU S5972. The relative position in time of the laser pulses with respect to the electron bunches is also influenced by an arrival time uncertainty due to the acceleration process [Win08]. Taking this into account, the timing jitter between the laser pulses and the electron bunches or the THz pulses respectively are estimated by former experiments to be in the order of 100 fs [Bre11, HSW+11, Sch12a, Sch12b].

5.4. Detection setup

A schematic of the setup for EO sampling in balanced detection is depicted in figure 5.5 and in addition, figure A.2 shows a photograph of this setup. The diameter of the optical breadboard mounted in the vacuum vessel is 100 cm. The vacuum vessel can be operated also in non-evacuated conditions by inserting an additional vacuum window to maintain the transfer line in evacuated conditions. Materials used during this work are TOPAS, a cyclic olefin copolymeric thermoplast [FHJW05], or z-cut crystalline quartz [RB67] providing a high transmission for THz radiation.

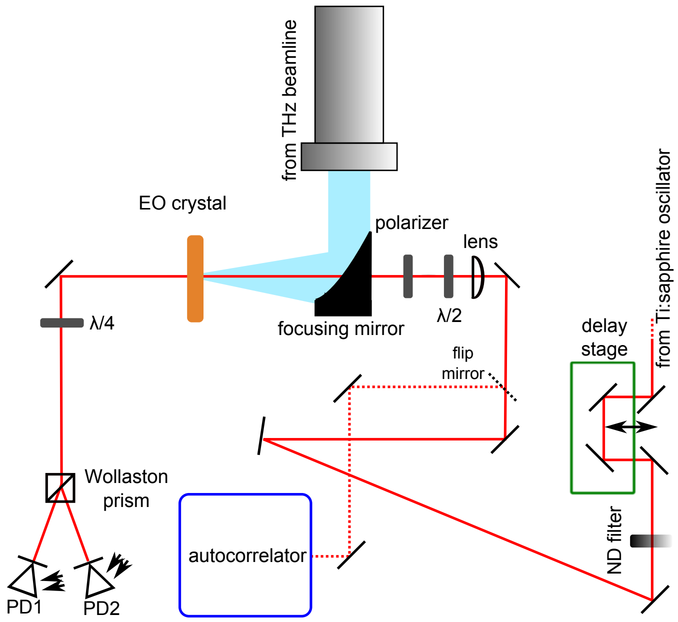

Figure 5.5.: Setup for EO sampling at the laboratory mounted in a vacuum vessel. Not to scale.

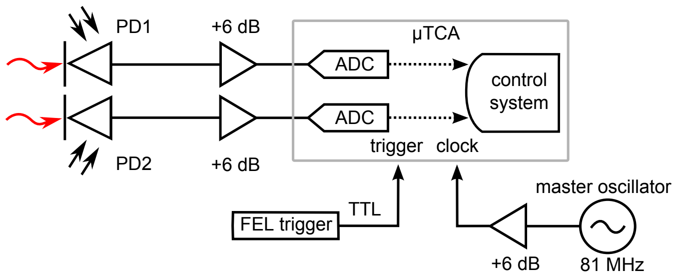

Figure 5.6.: Connection scheme of the read-out electronics. The laser intensities are acquired with photodetectors and digitized with an DESY AMC1 ADC, which is triggered on the FLASH electron bunches. The clock signal is generated by the RF distribution of the accelerator, to which the laser is locked.

5.5. Readout electronics

The analog signals of the two photodetectors (silicon detectors type THORLABS DET10A/M providing a rise time of 1 ns) are digitized with an ADC type DAMC1 developed at DESY [Smi11] operated in a μTCA crate [R+09]. The ADC provides a sampling frequency of $\frac{1.3\ \mathrm{GHz}}{16} = 81.25$ MHz synchronous with the RF signal distribution of the accelerator to which the laser is locked. Figure 5.6 shows a connection scheme of the read-out electronics. The trigger also delivered by the FLASH timing system gives a coarse temporal gate for the data acquisition of the ADC in the order of tens of nanoseconds. Since the CTR pulses are generated at 10 Hz, i.e. the bunch train repetition rate of the accelerator, but the laser pulses approach at the repetition rate of approx. 81 MHz, the trigger is used to identify the laser pulse which is going to be overlapped with the THz pulse. A method for fine timing is described in section 6.2. The raw data acquired are lists of ADC voltage signals for a specific time window of $2048 \cdot (81\ \mathrm{MHz})^{-1} \approx 25\ \mu\mathrm{s}$. These lists are imported into the FLASH control system DOOCS and accessible via MATHWORKS MATLAB [GGH+97]. Since the ADC clock is generated by the FLASH RF distribution to which the laser is synchronized, the list entry for one time step corresponds to the photodetector signal of one laser pulse. The relative position of the time window of one ADC sample to the photodetector signals is adjusted for a maximum ADC signal by inserting an additional delay line of cables.

6. Results

This chapter presents the results of the measurements using electro-optic sampling at the CTR source at FLASH. As one key device of this experiment, the laser system including its synchronization is characterized first. Then, measurements using electro-optic sampling of THz pulses for two crystals (ZnTe and GaP) are depicted and discussed and an error estimation is performed.

6.1. Characterization of the laser system

6.1.1. Spectrum and pulse length

The properties of spectral bandwidth and temporal length of the laser pulses are measured with commercial equipment. A fiber-coupled spectrometer APE WAVESCAN is used to acquire the spectrum – a result is depicted in fig. 6.1. The spectral width at full width at half maximum is 45 nm. The temporal width of the pulses is determined by autocorrelation of the laser pulses. In this technique, the laser beam is split in two parts. Spatially and temporally overlapped in an optically active crystal, the sum-frequency is generated. The intensity of the frequency sum gives the temporal convolution of the two components [DR06, Rul05]

$$I_{\mathrm{ACF}}(\tau) = \int_{-\infty}^{\infty} I(t) \cdot I(t-\tau) dt. \tag{6.1}$$

By delaying one part against the other, the time τ of evaluation of the convolution is changed and thus, the autocorrelation function (ACF) acquired. For typical pulse shapes for KERR mode-locked lasers, sech^2 pulses, the width (FWHM) of the autocorrelation function $\Delta\tau$ is larger by a factor of 1.543 compared to the FWHM width of the laser pulse Δt [CDC+95, Rul05].
The right plot of figure 6.1 shows the autocorrelation function acquired with an autocorrelator (APE PULSECHECK) (blue marks) with a fit according to sech^2 pulses

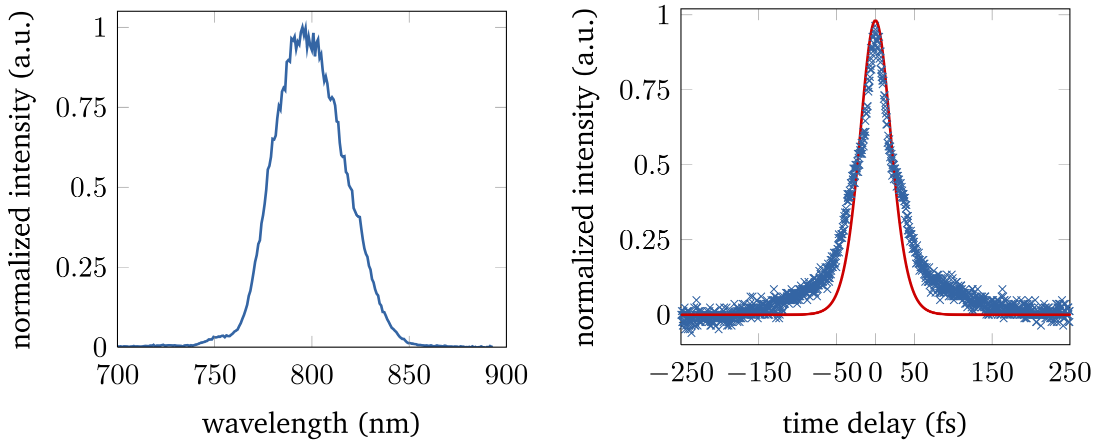

Figure 6.1.: (*Left*) Spectrum of laser pulses with $\Delta\lambda_{\mathrm{FWHM}} = 45$ nm. (*Right*) Autocorrelation function with a fit according to sech^2 pulses (*red*). The pulse duration (FWHM) is calculated from the ACF width to $\Delta t_{\mathrm{FWHM}} \approx 31$ fs. See text for details.

(red line). The temporal width is

$$\Delta t = \Delta\tau \cdot 1.543^{-1} \approx 47 \text{ fs } \cdot 1.543^{-1} \approx 30.5 \text{ fs}.$$

The "shoulders" of the autocorrelation function are caused by third-order dispersion acquired over the length of free-space beam transportation of approx. 5 m with several optical elements [Sch12b].

6.1.2. Synchronization

Beside the temporal laser pulse width, the arrival time stability of the laser pulse train is a major limitation of the resolution in time.

The *single-sideband* (SSB) *phase noise* [Sch12a] is an important indicator to estimate the timing stability. This quantity is acquired by comparison of the input signal to signals of reference oscillators implemented in the fully automated signal source analyzer (SSA). This phase noise also allows to estimate the quality of the phase-lock loop described in section 5.3.

The second important quantity derived from the SSB phase noise is the *integrated timing jitter* between the input signal and the reference oscillators in a defined frequency interval. The measurements depicted in this section are taken with a SSA

E5052B by AGILENT. The RF signal fed to the SSA is generated by the laser pulse train converted by an additional photodiode ET-4000F by EOT with a bandwidth larger than 12 GHz. The photodetector signal is processed by a 1.3 GHz band-pass filter and amplifiers similar to those used for the PLL (fig. 5.4).
Figures 6.2 and 6.3 show the SSB phase noise measurements for the free-running laser and with active PLL regulation, respectively. In both plots, the reference RF signal distributed by the FLASH master oscillator is also included (*grey*). The calculated integrated timing jitter values are given in table 6.1. Further measurements of this laser system can be found in [Sch12a].
The regulation operates in the range between 10 Hz and approx. 2 kHz. Comparing the SSB phase noise for the free-running and the locked laser, the fraction below 1 kHz is strongly suppressed by the regulation. The peak at 1.4 kHz which contains a large fraction of the integrated timing jitter is caused by the regulation and can be reduced by adjusting the regulation parameters, the *gain* settings [Sch12a].
For higher frequencies, the regulation increases the integrated timing jitter by imprinting additional noise. Sources are e.g. the piezo actuator with its driver electronics. The high-frequency components of the phase noise allow an estimation of the short-term timing stability. Due to limited bandwidth of the RF components, the fraction of the integrated timing jitter for offset frequencies above 10 MHz does not contribute to the measurement. It should be noted that these measurements do not allow the accurate determination of the timing jitter between the laser pulses and the electron bunches. Such a measurement is more complex, but can be conducted by bunch arrival time monitors available at FLASH [LAF+10, Boc12] in combination with electro-optic methods with a laser system locked to the optical reference oscillator [Sch12a]. However, the estimation of the timing jitter between the laser pulses and the electron bunches in the order of 100 fs is justified based on former experiments [Bre11, HSW+11, Sch12a, Sch12b].

Table 6.1.: Overview of the integrated timing jitter of the laser pulses in important offset frequency regimes. See text for details.

description	integrated timing jitter $\delta t_{\mathrm{rms}}(f)$ [ps] $f = [10\ \mathrm{Hz}, 1\ \mathrm{kHz}]$	$f = [1\ \mathrm{kHz}, 10\ \mathrm{MHz}]$
reference	0.066	0.039
free-running laser	11.9	0.041
locked laser	0.171	0.067

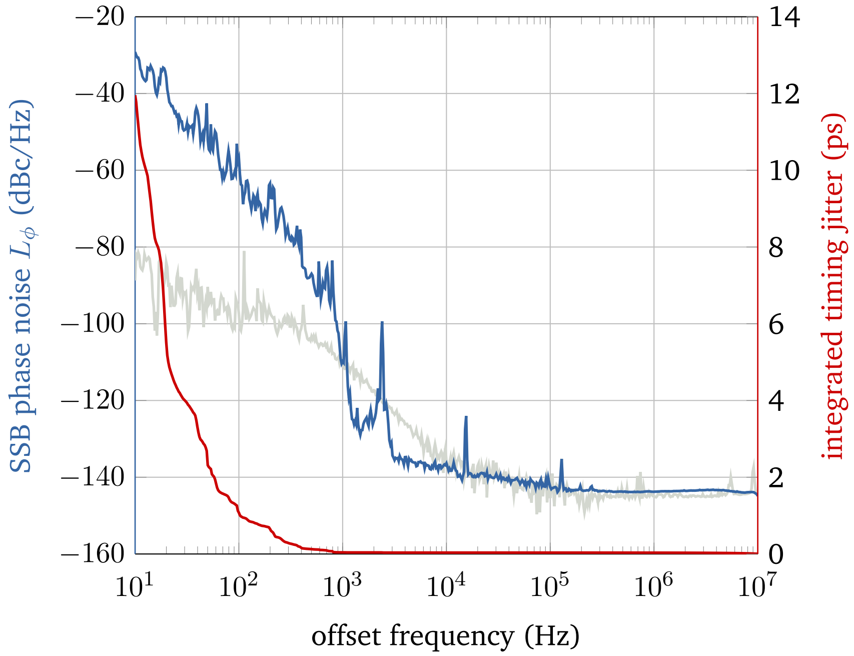

Figure 6.2.: SSB phase noise (*blue*) and integrated timing jitter (*red*) of the free-running laser. The RF reference signal is also included (*grey*).

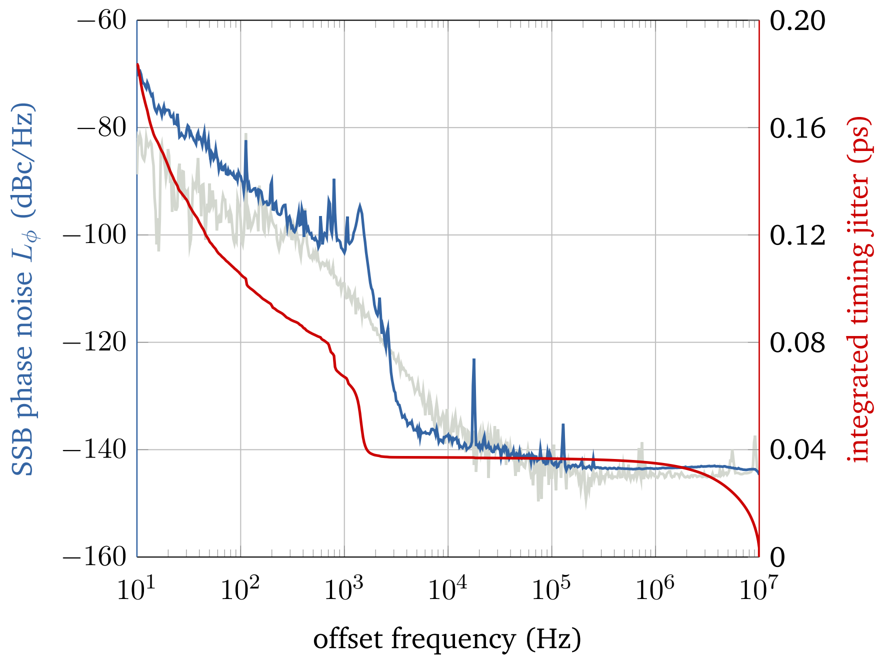

Figure 6.3.: SSB phase noise (*blue*) and integrated timing jitter (*red*) of the laser locked to the RF reference. The reference signal is also included (*grey*). Please note the different axis scales.

6.2. Electro-optic measurements

6.2.1. Timing search

A coarse temporal overlap between the laser pulses and the THz pulses is achieved using a mercury cadmium telluride (MCT) detector type VIGO PEM10.6, which is sensitive in the far-infrared and in the near-infrared regime. Both the signals of the laser pulses and the CTR pulses are observed on a 1 GHz oscilloscope TEKTRONIX DPO 4104 – figure A.3. By shifting the relative position of the laser pulses to the THz pulses using the digitally controlled vector modulator (VM) (fig. 5.4), an overlap of the rising edges of the MCT signals on the oscilloscope is established by visual judgment. A fine overlap can be established by scanning for the *electro-optic signal* using the VM as a first step and then the mechanical delay stage (type OWIS LTM 60F). Following equation (4.5) in chapter 5, the electro-optic signal is the modulation in the intensities, i.e. in the photodetector signals I_1 and I_2 also observed by visual judgment on the oscilloscope. An example is depicted in fig. A.4. When the fine temporal overlap has been set, the sampling measurements of the CTR pulses were conducted by continuous scanning with the delay stage. This mechanical stage has a movement range of 25 mm which corresponds to a maximum delay of approx. 167 ps due to the double pass on the stage indicated in fig. 5.5. The motor position and the time delay are calculated from the motor read-back delivered by the control system.

6.2.2. Data evaluation

From the raw ADC data described in section 5.5, the modulated pulses are picked and normalized to suppress amplitude noise using the mean of 20 non-modulated pulses. This data is used to calculate the phase retardation and in consequence the electric field strength according to eqn. (4.5) with an angle $\alpha = 0$ deg. To include the uncertainties of the laser synchronization and the motor velocity, the time delay axis is divided into bins of 100 fs width and the field strength data are averaged over one bin. The main sources for systematic error are discussed in section 6.2.6. The software MATHWORKS MATLAB R2009B and WOLFRAM MATHEMATICA 8 are used for the calculations.

6.2.3. ZnTe

In figure 6.4, an EO sampling measurement using a zinc telluride crystal of 300 μm thickness is presented. The most important electron beam parameters are:

$$\text{electron energy: } E = 684 \text{ MeV}$$
$$\text{bunch charge: } q = 450 \text{ pC.}$$

This measurement was conducted in the non-evacuated vacuum vessel and before the fine-tuning of the laser and THz beam alignment. Estimated with a pyroelectric detector (MICROTECH INSTRUMENTS), the spot size of the THz beam at the focus of the last parabolic mirror (fig. 5.5) is still in the order of one mm (details can be found in [CSS06]). The spatial overlap of the focus of the THz radiation and the laser spot on the crystal is varied to maximize the EO signal by adjusting this focusing mirror. Regarding figure 4.1 and equation (4.3), the angle α between the optically active crystal axis $\boldsymbol{X}$ and the electric field vector $\boldsymbol{E}_{\text{THz}}$ is also changed to find the optimal conditions. Following figure 4.2, the maximum signal emerges at $\alpha = 0$ deg. Beyond the non-optimized conditions described above, the single-cycle THz pulse is observable. The pulse of approx. 1 ps length is followed by oscillations due to the excitation of water vapor in the transfer line [XAS$^+$06] and the diamond window [DNC$^+$98].
During optimization the effect of over-rotation in phase retardation described in section 4.1 occurred using this crystal, so this crystal was replaced by a 200 µm thick GaP crystal.

6.2.4. GaP

For the same electron beam parameters, scans using a gallium phosphide crystal (thickness: 200 µm) have been conducted. Figure 6.5 shows a scan acquired by moving the delay stage in a range of 20 ps. The sampled temporal shape of single-cycle THz pulses has a peak field strength of 74 kV/cm and a width of approx. 0.9 ps. The spectrum of this pulse calculated with a FASTFOURIERTRANSFORM algorithm [BM67] is depicted in the top right of figure 6.5. The spectral bandwidth (FWHM) is approx. 1.2 THz. At 1.1 THz, an absorption line of water vapor is clearly observable.
For the measurements shown in figure 6.6, the polarization of the THz pulses is set by a wire-grid polarizer (MICROTECH INSTRUMENTS G25).
Regarding a non-perfect transmission of the polarizer, the horizontal polarization of the THz radiation has the same electric field strength compared to a trace without the polarizer (reference in figure 6.6), which is predicted for an angle $\alpha = 0$ deg. In contrast, a vertical polarization is not detected. This can be explained regarding

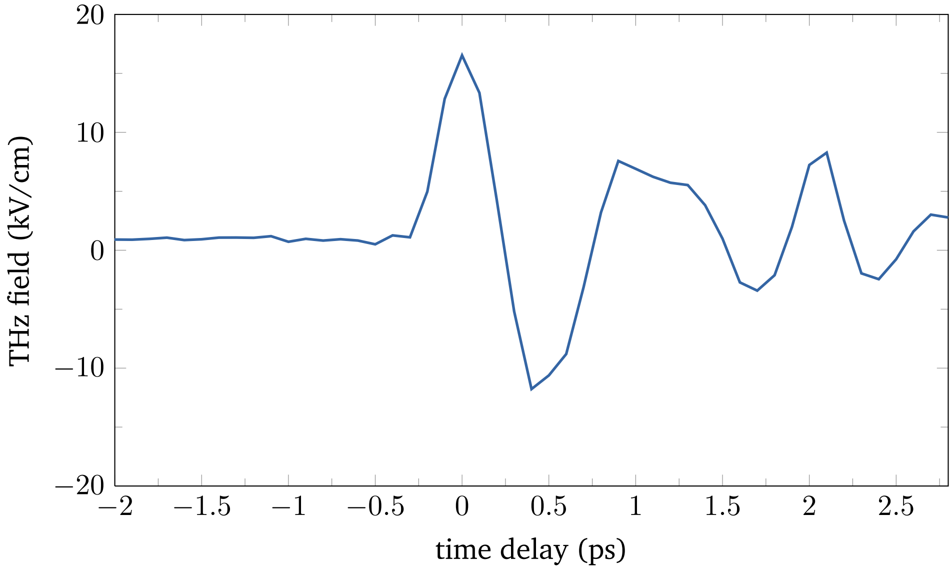

Figure 6.4.: THz pulse shape acquired with 0.3 mm ZnTe crystal.

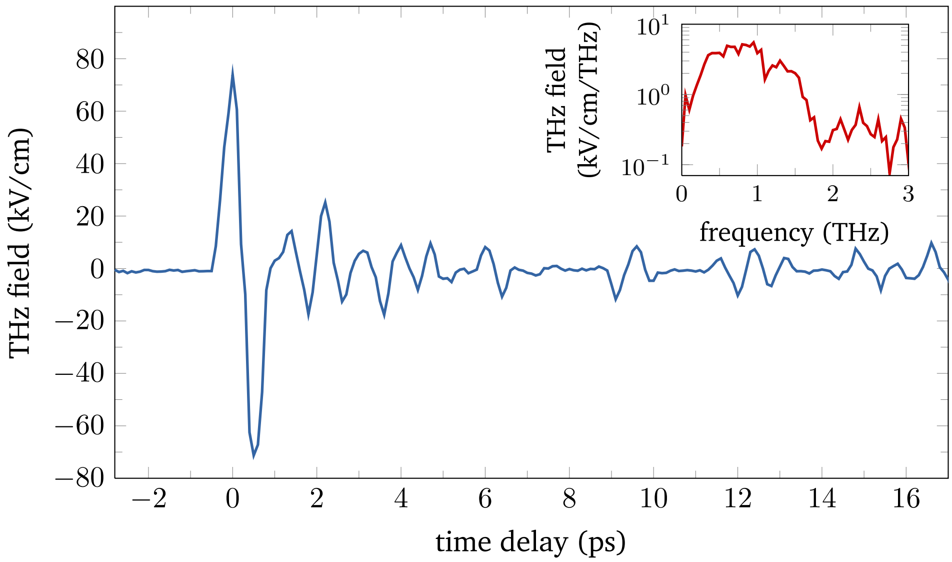

Figure 6.5.: Sampled THz pulse shape with a detection crystal of 200 µm GaP. The ringing behind the pulse (*right*) is due to the excitation of water vapor in the transfer line and the humid air. The plot in the top right shows the spectrum calculated using a FFT algorithm.

equation (4.3): for the vertical polarization, the angle α between the optically active axis $\boldsymbol{X}$ and the THz field vector $\boldsymbol{E}_{\mathrm{THz}}$ is $\pi/2$. Using equation (4.4), η becomes zero and the laser polarization is parallel to the major axis n_{s} of the index ellipse and thus, it experiences no phase retardation even though the vertical external electric field component is present. To overcome this, the crystal can the turned by $\pi/4$ around the axis perpendicular to the (110) plane, which leads again to an angle $\alpha = 0$ and $\eta = \pi/4$. For the polarization 45 deg, the imprint of the phase retardation on the laser pulses is not maximal. Following formula (4.4) for the orientation of the index ellipse in the (110) plane, the imprint is reduced to 70 % compared to the horizontal polarization at $\alpha = 0$. Taking this into account, the pulse for this polarization has a field strength comparible to the reference without the polarizer.

6.2.5. Measurements under vacuum conditions

Additionally to the results presented above, EO sampling measurements were also conducted using a 200 μm GaP crystal but in the evacuated vacuum vessel [HSW$^+$11]. In contrast to the usage of the mechanical scanning delay stage, the relative timing of the laser pulses to the THz pulses has been shifted with the vector modulator (VM). The electron beam parameters during this measurements are

$$\text{electron energy: } E = 697 \text{ MeV}$$
$$\text{bunch charge: } q = 420 \text{ pC.}$$

Figure 6.7 shows the sampled shape of THz pulses acquired by driving the VM in steps of 33 fs. Unlike the measurements described above, this plot shows the electric field strength averaged over 30 pulses for one VM step size. To avoid the effect of over-rotation, a pair of wire-grid polarizers of the type mentioned above attenuated the THz pulses by a factor of approx. 2. Taking into account this attenuation the peak field strength is 660 kV/cm. Regarding transmission losses in the two polarizers and amplitude distortion due to the jitter between the THz pulses and the laser pulses, the estimated peak field strength is in the order of 1 MV/cm and the single-cycle pulse has a duration of ≈ 500 fs [HSW$^+$11].

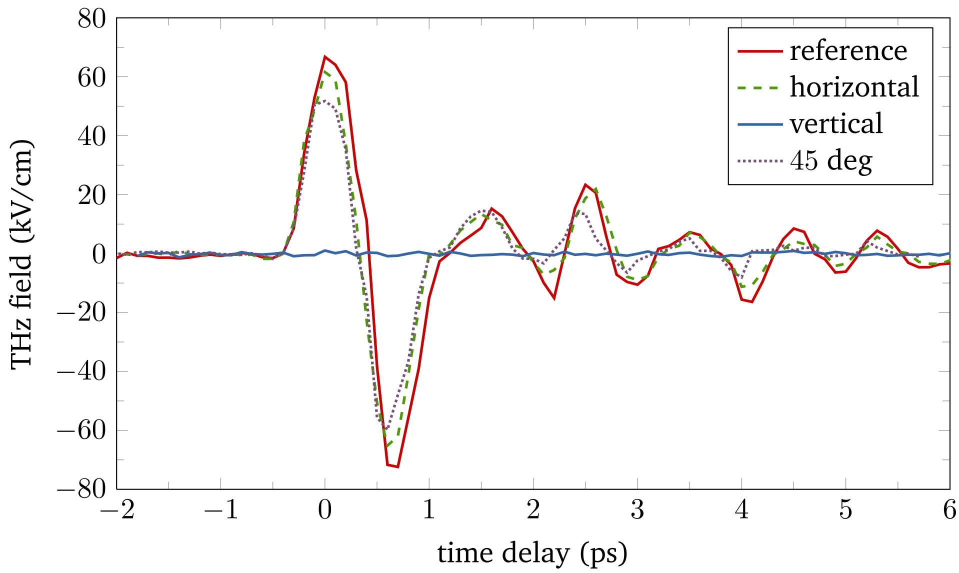

Figure 6.6.: THz pulses detected with a 0.2 mm GaP crystal for different polarizer settings including a reference (*red*) without the polarizer.

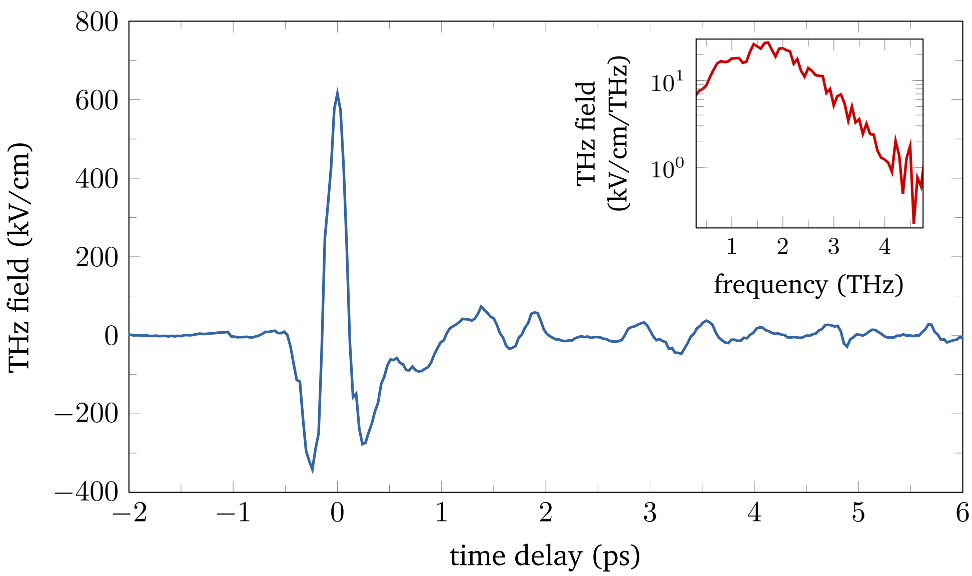

Figure 6.7.: Sampled THz pulses using a 0.2 mm GaP crystal under vacuum conditions. The plot in the top right shows the spectrum calculated by FFT. [HSW+11]

6.2.6. Error estimation

This experiment suffers primarily from the uncertainty of the timing stability between the electron bunches, i.e. the THz pulses and the laser pulses. As introduced in the previous sections, a determination of this quantity is complex but enabled by the implementation of the laser-based synchronization system at FLASH [Sch12a]. The synchronization of the laser system with the THz pulses in the order of 100 fs leads on the one hand to an averaging and in consequence to a reduction of the detected peak field strength. On the other hand, the distinction of temporal structures is only possible on this time scale. Due to this, the specification of systematic errors is rather complicated and can not be obtained during the measurements. In the following, the main error sources are discussed, i.e. the stability of the acceleration process, the sampling setup consisting of the laser system and the mechanical delay stage and the detection electronics. Table 6.2 summarizes the estimated error scales.
As introduced in chapter 2, the field strength of the CTR pulses scales with $Q_\mathrm{b}/\sqrt{s_\mathrm{b}}$ with the bunch charge Q_b and the bunch length s_b. The bunch charge is monitored by toroid coils [N+02] and the bunch length by BCMs, where the latter only allows a relative estimation of the bunch length fluctuation. The BCM signal, the intensity I_BCM of DR, scales with $Q_\mathrm{b}^2/s_\mathrm{b}$. Applying the error propagation formalism, the relative deviation from the mean of the CTR field $\sigma_{E_\mathrm{THz}}/E_\mathrm{THz}$ can be estimated by

$$\begin{aligned}\frac{\sigma_{E_\mathrm{THz}}}{E_\mathrm{THz}} &= \frac{\sigma_{Q_\mathrm{b}}}{Q_\mathrm{b}} + \frac{1}{2}\frac{\sigma_{s_\mathrm{b}}}{s_\mathrm{b}} \\ &= \frac{\sigma_{Q_\mathrm{b}}}{Q_\mathrm{b}} + \frac{1}{2}\left(\frac{\sigma_{I_\mathrm{BCM}}}{I_\mathrm{BCM}} - 2\frac{\sigma_{Q_\mathrm{b}}}{Q_\mathrm{b}}\right) \\ &= \frac{1}{2}\frac{\sigma_{I_\mathrm{BCM}}}{I_\mathrm{BCM}}.\end{aligned} \tag{6.2}$$

Figure 6.8 shows the relative deviation from mean of the THz field strength estimated with eqn. (6.2), where I_BCM is the intensity signal of BCM 4DBC3 and Q_b the bunch charge taken with the toroid coil 5DBC3 both located at the second bunch compressor BC3.
As depicted, the standard deviation of the fluctuation in electric field strength is 1.7 %. The electron bunch arrival time fluctuation leads directly to a fluctuation in time of the CTR pulses. Figure 6.10 shows the arrival time change of 1000 electron bunch trains used for the measurement depicted in fig. 6.5 acquired by the bunch arrival time monitor (BAM) near the CTR station. The standard deviation is ± 59 fs in this

measurement (*solid lines*). The BAM data can be used for a correction of the EO data [Boc12, LAF+10].

The noise on the ADC signals and the laser amplitude fluctuations is the third point of interest. As mentioned in section 6.2.2, 20 non-modulated pulses are used to overcome both the laser intensity and ADC noise and furthermore, differences in the absolute voltage amplitude of the photodetector signals of non-modulated pulses. In figure 6.9, the fluctuation of the ADC voltage signals for 1000 subsequent laser pulses for the two ADC channels is shown. As depicted, the standard deviation of the distribution is 1 %.

The next important point is the scanning device – the continuously-driven mechanical delay stage. The read-back values of the motor position are not instantaneously delivered by the control system, but at the rate of approx. 10 Hz. The time delay values are calculated from the motor position data. Referring to the specifications of the delay stage (OWIS LTM 60F) and the calculation of the time delay, the error of the time delay values is in the order of a few tens of femtoseconds.

For the measurement depicted in figure 6.5, this estimation leads to an error of ± 2 kV/cm at the peak field strength of 74 kV/cm and for the measurement under vacuum conditions (fig. 6.7) to ± 13 kV/cm at 660 kV/cm peak field strength.

Table 6.2.: Summary of the most important error sources in signal amplitudes and time. See text for details.

source	scale
in signal amplitudes:	
THz field strength	2%
laser amplitude and ADC noise	1%
in time:	
electron arrival time	60 fs
laser synchronization	100 fs
delay stage	20 fs
read-back calculation	20 fs

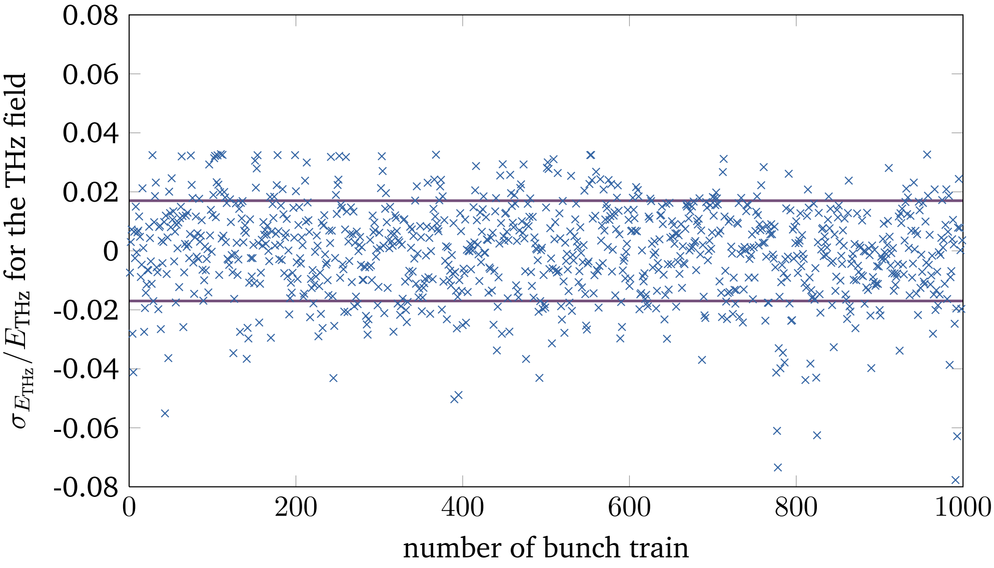

Figure 6.8.: Relative deviation of the electric field from mean calculated following eqn. (6.2). The data depicted here are for those electron bunches generating the sampled CTR pulses shown in fig. 6.5. The asymmetry can be explained by the behaviour of the pyro element of the BCM reaching the saturation. The solid lines indicate the standard deviation.

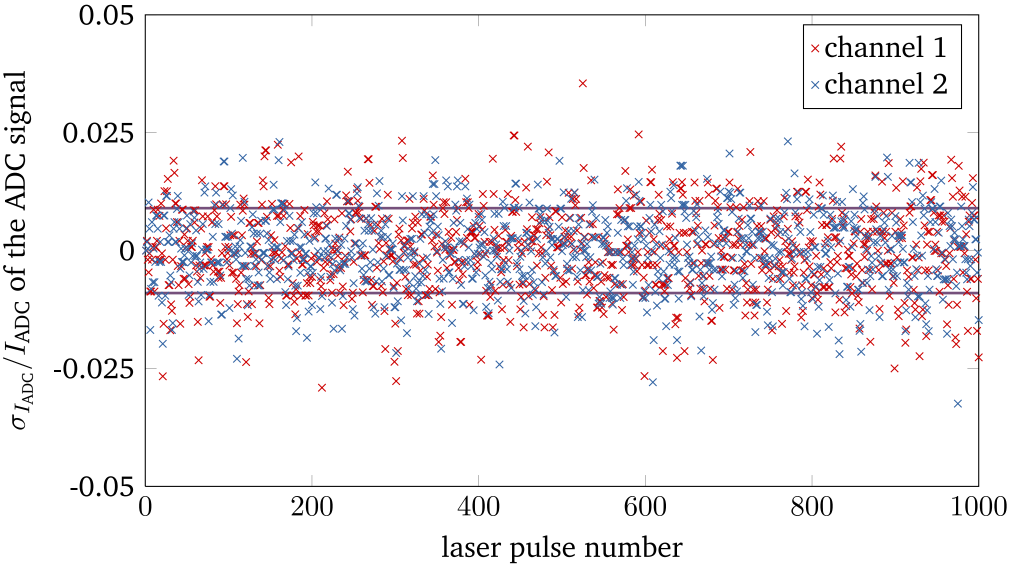

Figure 6.9.: Relative deviation of the ADC signal amplitude from mean value for the two ADC channels. The plot shows 1000 subsequent non-modulated laser pulses.

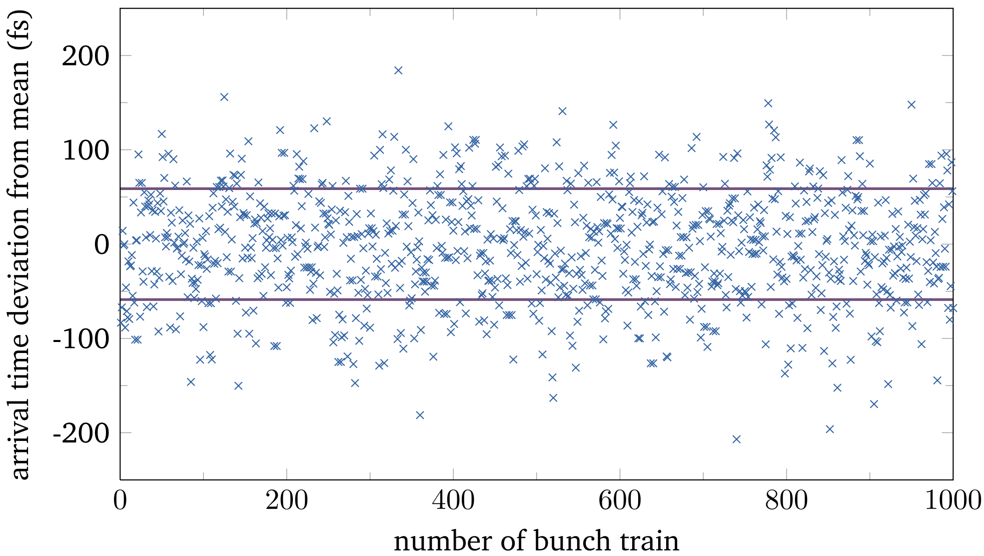

Figure 6.10.: Bunch arrival time fluctuation from the mean of 1000 bunch trains during the measurement depicted in fig. 6.5.

Conclusions and outlook

At the coherent transition radiation source at FLASH, radiation pulses have been characterized using the technique of electro-optic sampling. For this experiment, the transfer line guiding the CTR pulses from the accelerator into the external laboratory and the commercial titanium-sapphire laser system have been commissioned. A detection setup based on balanced detection has been installed and tested. Measurements with electro-optic crystals of zinc telluride and gallium phosphide delivered a quantitative and time-resolved determination of the electric field of the CTR pulses. The single-cycle pulses provide frequencies in the THz regime and the broadband and short pulses enable various experiments in a wide range of applications with field strengths in the focus in the order of 1 MV/cm. As introduced, the electric field strength depends on the electron bunches driving the CTR source, i.e. on bunch charge and length. In a next step the electron beam parameters are going to be optimized for maximum output power and field strength. In the near future, non-linear transmission and absorption experiments are going to be conducted at this source, which also enables more complex experiments including THz pump THz probe setups. The most important limitation in temporal resolution is the synchronization of the laser system with the accelerator. The current RF-based phase-lock loop is going to be extended with optical synchronization schemes available through the laser-based synchronization system at FLASH. With this, the timing jitter between the electron bunches and the laser pulses is expected to be in the order of a few tens of femtoseconds.

A. Photographs

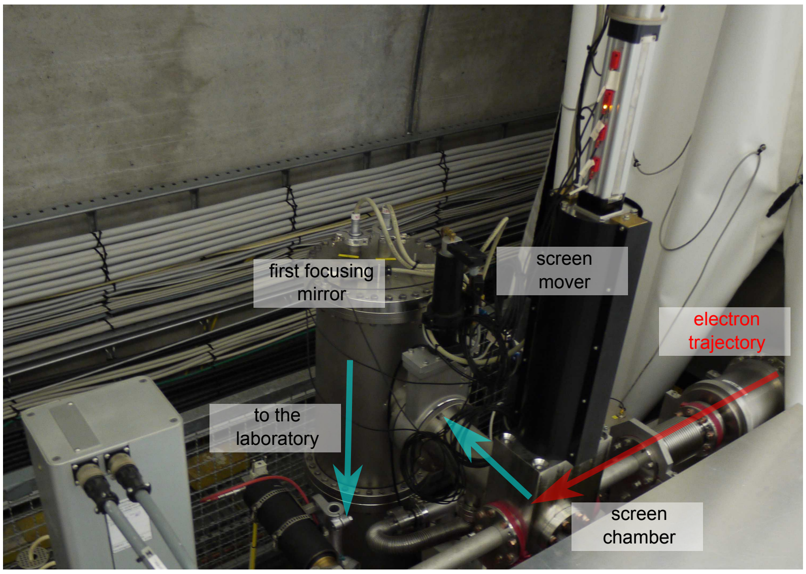

Figure A.1.: Photograph of the CTR station at the accelerator. The radiation is guided trough the transfer line beginning at the first focusing mirror into the external laboratory.

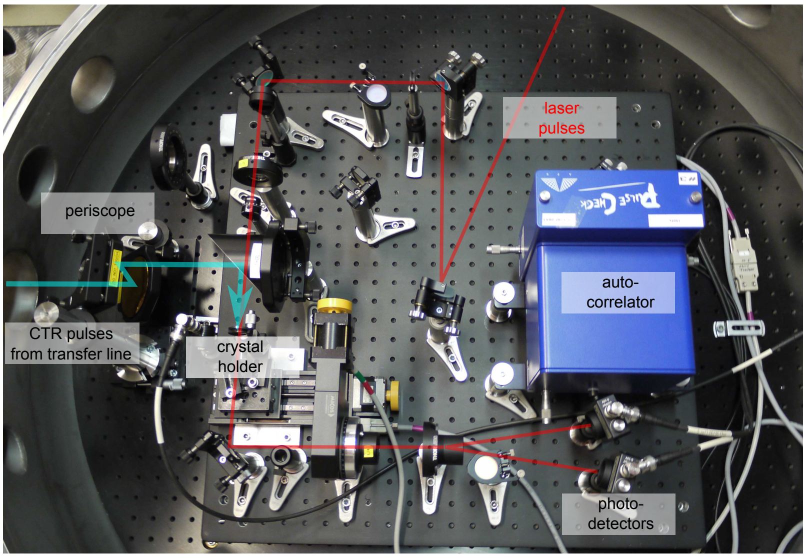

Figure A.2.: Photograph of the detection setup mounted in a vacuum vessel.

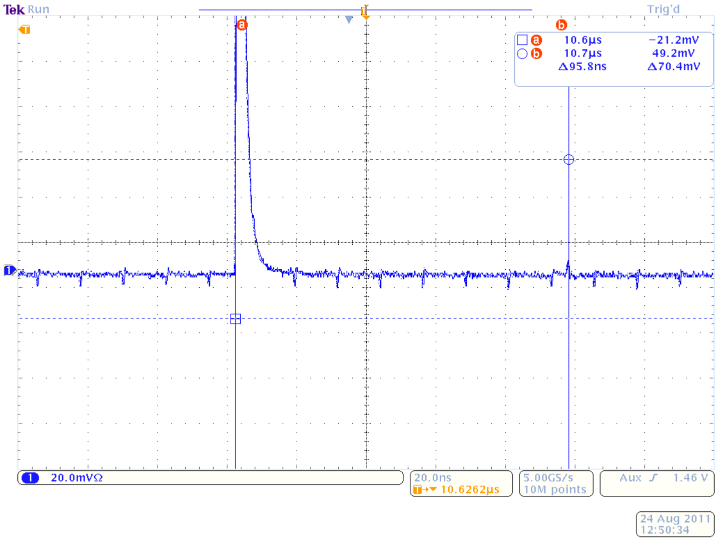

Figure A.3.: Oscilloscope display showing the laser pulses (*small negative dips*) and the CTR pulse (*huge positive signal*). By shifting the phase of the laser pulse train, a temporal overlap is achieved. The THz field is attenuated by a metal plate to avoid a saturation of the MCT.

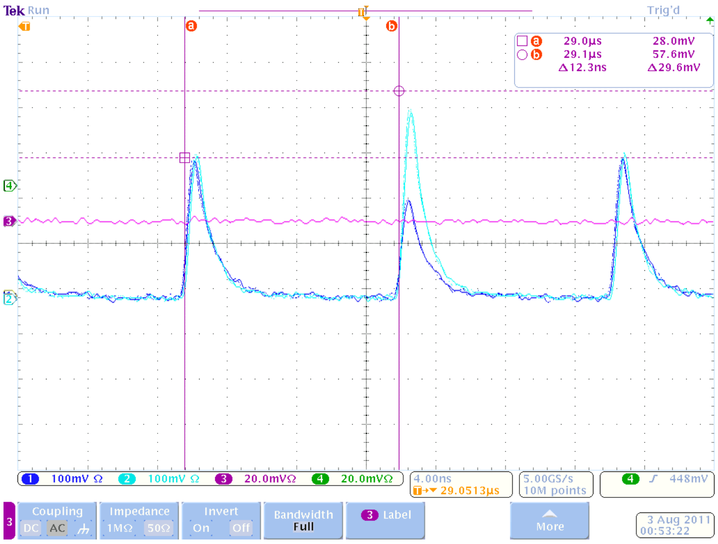

Figure A.4.: Electro-optic signal, the modulation in photodetector signals I_1 (*dark blue*) and I_2 (*light blue*) viewed on the oscilloscope (*center pulse*). (*Left / right pulse*): non-modulated laser pulses.

B. List of abbreviations

Table B.1.: List of abbreviations

ACC	accelerating module
ACF	autocorrelation function
ADC	analog to digital converter
BAM	bunch arrival time monitor
BC	bunch compressor
BCM	bunch compression monitor
CTR	coherent transition radiation
cw	continuous wave
DAC	digital to analog converter
DAMC	DESY advanced mezzanine card
DC	direct current
DESY	Deutsches Elektronen-Synchrotron
DFG	difference frequency generation
DR	diffraction radiation
DSP	digital signal processor
EO	electro-optic
eV	electronvolt
eqn	equation
FEL	free-electron laser
FELBE	FEL at the electron linear accelerator with high brilliance and low emittance
FELIX	free electron laser for infrared experiments
FFT	fast FOURIER transformation
fig	figure
FLASH	free-electron laser in Hamburg
FWHM	full width half maximum
GaAs	gallium arsenide

continued on next page

Table B.1.: List of abbreviations (*continued*)

GaP	gallium phosphide
GF	Ginzburg Frank
HOM	higher order harmonic
Hz	Hertz
InGaAs	indium gallium arsenide
InSb	indium antimonide
LESCO	$La_{1.675}Eu_{0.2}Sr_{0.125}CuO_4$
LN	lithium niobate
MBE	molecular beam epitaxy
MCT	mercury cadmium telluride
µTCA	micro telecommunications computing architecture
MO	master oscillator
n/a	not available
ND	neutral density
OR	optical rectification
PD	photodetector
PLL	phase-lock loop
RF	radio frequency
rms	root mean square
SASE	self-amplified spontaneous emission
sec	section
SSA	signal source analyzer
SSB	single side band
TDS	transverse deflecting structure
Ti:Sa	titanium-doped sapphire
TR	transition radiation
TTL	transistor-transistor logic
VM	vector modulator
VUV	vacuum ultraviolet
XUV	extreme ultraviolet
Yb	ytterbium
ZnTe	zinc telluride

Bibliography

[ABB$^+$00] B. Aune, R. Bandelmann, D. Bloess, B. Bonin, A. Bosotti, M. Champion, C. Crawford, et al., *Superconducting TESLA cavities*, Physical Review Special Topics - Accelerators and Beams **3** (2000), no. 9.

[ALL64] O. H. Altenmueller, R. R. Larsen, and G. a. Loew, *Investigations of Traveling-Wave Separators for the Stanford Two-Mile Linear Accelerator*, Review of Scientific Instruments **35** (1964), no. 4, 438.

[AS83a] D. Aspnes and A. Studna, *Dielectric functions and optical parameters of Si, Ge, GaP, GaAs, GaSb, InP, InAs, and InSb from 1.5 to 6.0 eV*, Physical Review B **27** (1983), no. 2, 985–1009.

[AS83b] D. H. Auston and P. R. Smith, *Generation and detection of millimeter waves by picosecond photoconductivity*, Applied Physics Letters **43** (1983), no. 7, 631.

[BAC$^+$10] J. Bödewadt, A. Azima, F Curbis, H. Delsim-Hashemi, M. Drescher, E. Hass, U. Hipp, T. Maltezopoulos, V. Miltchev, M. Mittenzwey, M. Rehders, J. Rossbach, J. Rönsch-Schulenburg, R. Tarkeshian, M. Wieland, S. Bajt, S. Düsterer, K. Honkavaara, T. Laarmann, H. Schlarb, S. Khan, and R. Ischebeck, *sFLASH - First results of direct seeding at FLASH*, Proceedings of the 32th free-electron laser conference, 2010, pp. 330–335.

[Beh08] C. Behrens, *Detection and Spectral Measurements of Coherent Synchrotron Radiation at FLASH*, Diploma thesis, University of Hamburg, 2008.

[Beh10] C. Behrens, *Simulations on Beam Monitor Systems and Longitudinal Feedback Schemes for FLASH*, Talk held on the 48th ICFA Advanced Beam Dynamics Workshop on Future Light Sources, FLS 2010, Working Group 6, 2010.

[BFWW62] M. Bass, P. A. Franken, F. Ward, and G. Weinreich, *Opical Rectification*, Physical Review Letters **9** (1962), no. 11, 28–31.

[BGG$^+$12] C. Behrens, N. Gerasimova, Ch. Gerth, B. Schmidt, E. A. Schneidmiller, S. Wesch, M. V. Yurkov, and S. Serkez, *Constraints on Photon Pulse Duration from Longitudinal Electron Beam Diagnostics at a Soft X-ray Free-electron Laser*, TESLA FEL Report **01** (2012).

[BM67] E. O. Brigham and R. E. Morrow, *The fast fourier transform*, Spectrum, IEEE **4** (1967), no. 12, 63–70.

[BMNC89] Y. Berozashvili, S. Machavariani, A. Natsvlishvili, and A. Chirakadze, *Dispersion of the linear electro-optic coefficients and the non-linear susceptibility in GaP*, Journal of Physics D: Applied Physics **22** (1989), no. 22, 682.

[Boc12] M. K. Bock, *Measuring the Electron Bunch Timing with Femtosecond Resolution at FLASH*, 2012. PhD thesis, University of Hamburg, **to be published.**

[Bre11] J. Breunlin, *Commissioning of an Electro-Optic Electron Bunch Length Monitor at FLASH*, Diploma thesis, University of Hamburg, 2011.

[BSK+10] M. Beck, H. Schäfer, G. Klatt, J. Demsar, S. Winnerl, M. Helm, and T. Dekorsy, *Impulsive terahertz radiation with high electric fields from an amplifier-driven large-area photoconductive antenna*, Optics Express **18** (2010), no. 9, 9251.

[BSWN10] C. Behrens, B. Schmidt, S. Wesch, and D. Nicoletti, *Upgrade and evaluation of the bunch compression monitor at the free-electron laser in Hamburg (FLASH)*, Proceedings of the 1st International Particle Accelerator Conference, 2010, pp. 912–914.

[CCOV99] M. Castellano, A. Cianchi, G. Orlandi, and V. A. Verzilov, *Effects of diffraction and target finite size on coherent transition radiation spectra in bunch length measurements*, Nuclear Instruments and Methods in Physics Research Section A: Accelerators, Spectrometers, Detectors and Associated Equipment **435** (1999), no. 3, 297–307.

[CDC+95] P. F. Curley, G. Darpentigny, G. Cheriaux, J. P. Chambaret, and A. Antonetti, *High dynamic range autocorrelation studies of a femtosecond Ti: sapphire oscillator and its relevance to the optimisation of chirped pulse amplification systems*, Optics Communications **120** (1995), no. 1–2, 71–77.

[CJW+04] M. Chamberlain, B. Jones, I. Wilke, G. Williams, B. Parks, T. Heinz, and P. Siegel, *Opportunities in THz Science*, DOE-NSF-NIH Workshop, 2004.

[Cla04] J. A. Clarke, *The science and technology of undulators and wigglers*, Oxford University Press, 2004.

[CSS05] S. Casalbuoni, B. Schmidt, and P. Schmüser, *Far-Infrared Transition and Diffraction Radiation Part I: Production, Diffraction Effects and Optical Propagation*, TESLA Report **15** (2005).

[CSS06] S. Casalbuoni, B. Schmidt, and P. Schmüser, *Far-Infrared Transition and Diffraction Radiation Part II: The THz Beamline at the VUV-FEL Linac Basic Design Criteria of the THz Beamline*, TESLA FEL Report **04** (2006).

[CSS+09] S. Casalbuoni, B. Schmidt, P. Schmüser, V. Arsov, and S. Wesch, *Ultrabroadband terahertz source and beamline based on coherent transition radiation*, Physical Review Special Topics - Accelerators and Beams **12** (2009), no. 3, 030705.

[DGF+11] D. Daranciang, J. Goodfellow, M. Fuchs, H. Wen, S. Ghimire, D. A. Reis, H. Loos, A. S. Fisher, and A. M. Lindenberg, *Single-cycle terahertz pulses with >0.2 V/Å field amplitudes via coherent transition radiation*, Applied Physics Letters **99** (2011), no. 14, 141117.

[DNC+98] P. Dore, A. Nucara, D. Cannavo, G. De Marzi, P. Calvani, A. Marcelli, R. S. Sussmann, A. J. Whitehead, C. N. Dodge, A. J. Krehan, et al., *Infrared properties of chemical-vapor deposition polycrystalline diamond windows*, Applied Optics **37** (1998), no. 24, 5731–5736.

[DR06] J.-C. Diels and W. Rudolph, *Ultrashort Laser Pulse Phenomena*, 2nd ed., Academic Press, 2006.

[EBH10] H. Edwards, C. Behrens, and E. Harms, *3.9 GHz cavity module for linear bunch compression at FLASH*, Proceedings of the 25th International Linear Accelerator Conference, 2010.

[FHJW05] B. Fischer, M. C. Hoffmann, U. P. Jepsen, and M. Walther, *Use of the plastic materials topas and zeonex for biotechnological applications in the terahertz range*, European Patent Application EP1505382 (2005).

[FP99] B. Faatz and J. Pflüger, *Magnet Sorting for the TTF-FEL Undulator using Simulated Annealing*, TESLA FEL report **01** (1999).

[Frü09] U. Frühling, *Lichtfeld getriebene Streak-Kamera zur Einzelschuss Zeitstrukturmessung der XUV-Pulse eines Freie-Elektronen Lasers*, PhD thesis, University of Hamburg, 2009.

[FTD+11] D. Fausti, R. I. Tobey, N. Dean, S. Kaiser, A. Dienst, M. C. Hoffmann, S. Pyon, T. Takayama, H. Takagi, and A. Cavalleri, *Light-induced superconductivity in a stripe-ordered cuprate.*, Science **331** (2011), no. 6014, 189–191.

[FWG+09] U. Fruhling, M. Wieland, M. Gensch, T. Gebert, B. Schutte, M. Krikunova, R. Kalms, F. Budzyn, O. Grimm, J. Rossbach, E. Plönjes, and M. Drescher, *Single-shot terahertz-field-driven X-ray streak camera*, Nature Photonics **3** (2009), no. 9, 523–528.

[GGH+97] S. Goloborodko, G. Grygiel, O. Hensler, V. Kocharyan, K. Rehlich, and P. Shevtsov, *DOOCS: an Object Oriented Control System as the Integrating Part for the TTF Linac*, Proceedings of the International Conference on Accelerator and Large Experimental Physics Control Systems, 1997.

[Gob87] H. Gobrecht (ed.), *Bergmann Schaefer Lehrbuch der Experimentalphysik*, 8th ed., Vol. 3, de Gruyter, 1987.

[Gri99] D. J. Griffiths, *Introduction to Electrodynamics*, 3rd ed., Prentice Hall, 1999.

[GTKC70] T. K. Gustafson, J.-P. E. Taran, P. L. Kelley, and R. Y. Chiao, *Self-modulation of picosecond pulses in electro-optic crystals*, Optics Communications **2** (1970), no. 1, 17–21.

[HDBT11] H. Hirori, A. Doi, F. Blanchard, and K. Tanaka, *Single-cycle terahertz pulses with amplitudes exceeding 1 MV/cm generated by optical rectification in LiNbO3*, Applied Physics Letters **98** (2011), no. 9, 091106.

[HF11] M. C. Hoffmann and J. A. Fülöp, *Intense ultrashort terahertz pulses: generation and applications*, Journal of Physics D: Applied Physics **44** (2011), no. 8, 083001.

[HHH+09] M. C. Hoffmann, J. Hebling, H. Y. Hwang, K.-L. Yeh, and K. A. Nelson, *THz-pump/THz-probe spectroscopy of semiconductors at high field strengths [Invited]*, J. Opt. Soc. Am. B **26** (2009), no. 9, 29–34.

[HSB91] U. Happek, A. J. Sievers, and E. B. Blum, *Observation of coherent transition radiation*, Physical review letters **67** (1991), no. 21, 2962–2965.

[HSW+11] M. C. Hoffmann, S. Schulz, S. Wesch, S. Wunderlich, A. Cavalleri, and B. Schmidt, *Coherent single-cycle pulses with MV/cm field strengths from a relativistic transition radiation light source.*, Optics letters **36** (2011), no. 23, 4473–5.

[Isc03] R. Ischebeck, *Transverse Coherence of a VUV Free Electron Laser*, PhD thesis, University of Hamburg, 2003.

[Jac75] J. D. Jackson, *Classical Electrodynamics*, 2nd ed., Wiley & Sons, 1975.

[Löh09] F. Löhl, *Optical Synchronization of a Free-Electron Laser with Femtosecond Precision*, PhD thesis, University of Hamburg, 2009.

[LAF+10] F. Löhl, V. Arsov, M. Felber, K. Hacker, W. Jalmuzna, B. Lorbeer, F. Ludwig, K.-H. Matthiesen, H. Schlarb, B. Schmidt, P. Schmüser, S. Schulz, J. Szewinski, A. Winter, and J. Zemella, *Electron Bunch Timing with Femtosecond Precision in a Superconducting Free-Electron Laser*, Physical Review Letters **104** (2010), no. 14, 144801.

[LC00] H. C. Liu and F. Capasso, *Semiconductors and semimetals Volume 62: Intersubband transitions in quantum wells : physics and device applications I*, Academic Press, 2000.

[LIW03] H. Lim, F. Ö. Ilday, and F. W. Wise, *Generation of 2-nJ pulses from a femtosecond ytterbium fiber laser.*, Optics letters **28** (2003), no. 8, 660–662.

[LS97] R. Lai and A. J. Sievers, *On using the coherent far IR radiation produced by a charged-particle bunch to determine its shape: I Analysis*, Nuclear Instruments and Methods in Physics Research Section A: Accelerators, Spectrometers, Detectors and Associated Equipment **397** (1997), no. 2-3, 221–231.

[MGG+04] P. Michel, F. Gabriel, E. Grosse, P. Evtushenko, T. Dekorsy, M. Krenz, M. Helm, U. Lehnert, W. Seidel, D. Wohlfarth, and A. Wolf, *First lasing of the ELBE MID-IR FEL*, Proceedings of the 26th free-electron laser conference, 2004.

[Mou82] P. F. Moulton, *Ti-doped sapphire: tunable solid-state laser*, Optics News **8** (1982), no. 6, 9.

[Mou86] P. F. Moulton, *Spectroscopic and laser characteristics of Ti:Al2O3*, Journal of the Optical Society of America B **3** (1986), no. 1, 125–133.

[N+02] D. Nölle et al., *The diagnostic system of TTF II*, Proceedings of 8th European Particle Accelerator Conference, 2002.

[PMR+08] B. Pradarutti, G. Matthaus, S. Riehemann, G. Notni, S. Nolte, and A. Tunnermann, *Highly efficient terahertz electro-optic sampling by material optimization at 1060nm*, Optics Communications **281** (2008), no. 19, 5031–5035.

[RB67] E. E. Russell and E. E. Bell, *Measurement of the Optical Constants of Crystal Quartz in the Far Infrared with the Asymmetric Fourier-Transform Method*, Journal of Optical Society of America **57** (1967), no. 3, 341–348.

[R+09] K. Rehlich et al., *New Hardware and Software Developments for the XFEL*, Proceedings of the International Conference on Accelerator and Large Experimental Physics Control Systems, 2009.

[Rul05] C. Rulliere, *Femtosecond laser pulses: principles and experiments*, Springer Verlag, 2005.

[Sch06] B. Schmidt, *Overview on diagnostics for X-and XUV-FEL*, Proceedings of the 28th free-electron laser conference, 2006, pp. 761–768.

[Sch10] J. R. Schneider, *FLASH - from accelerator test facility to the first single-pass soft x-ray free-electron laser*, Journal of Physics B: Atomic, Molecular and Optical Physics **43** (2010), no. 19, 194001.

[Sch12a] S. Schulz, *Implementation of the Laser-Based Femtosecond Precision Synchronization System at FLASH*, 2012. PhD thesis, University of Hamburg, **to be published.**

[Sch12b] S. Schulz, *(seb.schulz@desy.de). Private communication.* (2012).

[SDR08] P. Schmüser, M. Dohlus, and J. Rossbach, *Ultraviolet and Soft X-Ray Free-Electron Lasers*, Springer Tracts in Modern Physics, vol. 229, Springer Berlin Heidelberg, 2008.

[SFF+10] S. Schreiber, B. Faatz, J. Feldhaus, K. Honkavaara, R. Treusch, M. Vogt, and J. Rossbach, *FLASH upgrade and first results*, Proceedings of the 32th free-electron laser conference, 2010, pp. 198–201.

[Smi11] P. Smirnov, *(petr.smirnov@desy.de). Private communication.* (2011).

[SR10] F. Sizov and A. Rogalski, *THz detectors*, Progress in Quantum Electronics **34** (2010), no. 5, 278–347.

[Ste07] B. R. Steffen, *Electro-Optic Methods for Longitudinal Bunch Diagnostics at FLASH*, PhD thesis, University of Hamburg, 2007.

[Stu04] F. Stulle, *A Bunch Compressor for small Emittances and high Peak Currents at the VUV Free-Electron Laser*, PhD thesis, University of Hamburg, 2004.

[TMKF92] K. Takami, T. Matsuyama, K. Kobayashi, and Y. Fujita, *Observation of coherent transition radiation at millimeter and submillimeter wavelengths*, Physical Review A **45** (1992), no. 12, 8340–8343.

[Van04] A. F. G. Van Der Meer, *FELs, nice toys or efficient tools?*, Nuclear Instruments and Methods in Physics Research Section A: Accelerators, Spectrometers, Detectors and Associated Equipment **528** (2004), no. 12, 8 –14.

[VGK+06] N. A. Vinokurov, N. G. Gavrilov, B. A. Knyazev, E. I. Kolobanov, V. V. Kotenkov, V. V. Kubarev, G. N. Kulipanov, A. N. Matveenko, L. E. Medvedev, S. V. Miginsky, et al., *Status of the Novosibirsk high power terahertz FEL*, Talk held at the 28th free-electron laser conference, 2006.

[Vod06] K. L. Vodopyanov, *Optical generation of narrow-band terahertz packets in periodically inverted electro-optic crystals: conversion efficiency and optimal laser pulse format.*, Optics Express **14** (2006), no. 6, 2263–2276.

[War91] L. Ward, *Zinc Telluride (ZnTe)* (E. D. Palik, ed.), Academic Press, San Diego, 1991.

[Wes08] S. Wesch, *Spektroskopie kohärenter Übergangsstrahlung zur Strukturanalyse von Elektronenpaketen am FLASH-Beschleuniger*, Diploma thesis, University of Hamburg, 2008.

[Wes12] S. Wesch, *Echtzeitbestimmung longitudinaler Elektronenstrahlparameter mittels absoluter Intensitäts- und Spektralmessung einzelner kohärenter THz Strahlungspulse*, 2012. PhD thesis, University of Hamburg, **to be published.**

[Wil08] A. Willner, *Investigations into the FLASH Infrared Undulator as an Electron Beam Diagnostic Tool*, Diploma thesis, University of Hamburg, 2008.

[Win08] A. Winter, *Fiber Laser Master Oscillators for Optical Synchronization Systems*, PhD thesis, University of Hamburg, 2008.

[Wiß12] L.-G. Wißmann, *A Robust Fibre Laser System for Electro-Optic Electron Bunch Profile Measurements at FLASH*, 2012. PhD thesis, University of Hamburg, **to be published.**

[WSB+11] S. Wesch, B. Schmidt, C. Behrens, H. Delsim-Hashemi, and P. Schmüser, *A multi-channel THz and infrared spectrometer for femtosecond electron bunch diagnostics by single-shot spectroscopy of coherent radiation*, Nuclear Instruments and Methods in Physics Research Section A: Accelerators, Spectrometers, Detectors and Associated Equipment **665** (2011), 40–47.

[WZ96] Q. Wu and X.-C. Zhang, *Ultrafast electro-optic field sensors*, Applied Physics Letters **68** (1996), no. 12, 1604.

[XAS+06] X. Xin, H. Altan, A. Saint, D. Matten, and R. Alfano, *Terahertz absorption spectrum of para and ortho water vapors at different humidities at room temperature*, Journal of Applied Physics **100** (2006), 094905.

Acknowledgments – Danksagungen

Danken möchte ich an dieser Stelle

- Herrn Dr. Bernhard Schmidt für die Möglichkeit der Anfertigung dieser Diplomarbeit in der Gruppe FLA bei DESY sowie die Ratschläge und das vermittelte Wissen in vielen Diskussionen und Gesprächen
- Herrn Dr. Jens Osterhoff und Herrn Prof. Dr. Jörg Rossbach für das geweckte Interesse an der Beschleunigerphysik sowie
- Herrn Dr. Matthias C. Hoffmann für mein Interesse an THz-Strahlung und die praktische Arbeit im Labor.
- Laurens für die Anregungen, die vielen wertvollen und ertragreichen Gespräche
- Christopher, Eugen, Sebastian und Stephan für stets die richtige Antwort auf meine Fragen
- und allen Mitgliedern der Gruppe FLA für die freundliche Aufnahme in die Arbeitsgruppe, die technischen Problemlösungen, organisatorischen Hilfeleistungen und die angenehmen Gespräche und Diskussionen!
- sowie allen Unerwähnten, die mich im Studium unterstützt haben!